Iodine oxoacids enhance nucleation of sulfuric acid particles in the atmosphere. 382, 1308-1314 (2023). DOI: 10.1126/science.adh2526 (https://www.science.org/doi/10.1126/science.adh2526).

The data for the figures can be found on https://zenodo.org/record/8344386.

Title: Iodine oxoacids enhance nucleation of sulfuric acid particles in the atmosphere

Authors:

Xu-Cheng He[1,2,3*], Mario Simon[4], Siddharth Iyer[5], Hong-Bin Xie[6*], Birte Rörup[1], Jiali Shen[1], Henning Finkenzeller[7,8], Dominik Stolzenburg[1,9], Rongjie Zhang[6], Andrea Baccarini[10,11], Yee Jun Tham[1,12], Mingyi Wang[13], Stavros Amanatidis[13], Ana A. Piedehierro[3], Antonio Amorim[14], Rima Baalbaki[1], Zoé Brasseur[1], Lucía Caudillo[4], Biwu Chu[1,15], Lubna Dada[1,10], Jonathan Duplissy[1,16], Imad El Haddad[10], Richard C Flagan[13], Manuel Granzin[4], Armin Hansel[17], Martin Heinritzi[4], Victoria Hofbauer[2], Tuija Jokinen[1,18], Deniz Kemppainen[1], Weimeng Kong[13], Jordan Krechmer[19], Andreas Kürten[4], Houssni Lamkaddam[10], Brandon Lopez[2,20], Fangfang Ma[6], Naser G. A. Mahfouz[2], Vladimir Makhmutov[21,22], Hanna E. Manninen[23], Guillaume Marie[4], Ruby Marten[10], Dario Massabò[24], Roy L. Mauldin[25,26], Bernhard Mentler[17], Antti Onnela[23], Tuukka Petäjä[1], Joschka Pfeifer[23], Maxim Philippov[21], Ananth Ranjithkumar[27], Matti P. Rissanen[5,28], Siegfried Schobesberger[29], Wiebke Scholz[17], Benjamin Schulze[13], Mihnea Surdu[10], Roseline C. Thakur[1], António Tomé[30], Andrea C. Wagner[4], Dongyu Wang[10], Yonghong Wang[1,15], Stefan K. Weber[23,4], André Welti[3], Paul M. Winkler[31], Marcel Zauner-Wieczorek[4], Urs Baltensperger[10], Joachim Curtius[4], Theo Kurtén[28], Douglas R. Worsnop[1,19], Rainer Volkamer[7,8], Katrianne Lehtipalo[1,3], Jasper Kirkby[23,4], Neil M. Donahue[2,20,25,32], Mikko Sipilä[1*], Markku Kulmala[1,16,33,34*]

Affiliations:

[1]Institute for Atmospheric and Earth System Research/Physics, Faculty of Science, University of Helsinki; 00014 Helsinki, Finland.
[2]Center for Atmospheric Particle Studies, Carnegie Mellon University; Pittsburgh, 15213 PA, USA.
[3]Finnish Meteorological Institute; 00560 Helsinki, Finland.
[4]Institute for Atmospheric and Environmental Sciences, Goethe University Frankfurt; 60438 Frankfurt am Main, Germany.
[5]Aerosol Physics Laboratory, Faculty of Engineering and Natural Sciences, Tampere University; 33720 Tampere, Finland.
[6]Key Laboratory of Industrial Ecology and Environmental Engineering (Ministry of Education), School of Environmental Science and Technology, Dalian University of Technology; 116024 Dalian, China
[7]Department of Chemistry, University of Colorado Boulder; Boulder, CO 80309, USA.
[8]Cooperative Institute for Research in Environmental Sciences, University of Colorado Boulder; Boulder, CO 80309, USA.
[9]Institute for Materials Chemistry, TU Wien; 1060 Vienna, Austria.
[10]Laboratory of Atmospheric Chemistry, Paul Scherrer Institute; CH-5232 Villigen, Switzerland.
[11]Laboratory of Atmospheric Processes and their Impact, Ecole Polytechnique Fédérale de Lausanne (EPFL); 1015 Lausanne, Switzerland.
[12]School of Marine Sciences, Sun Yat-sen University; 519082 Zhuhai, China.
[13]Division of Chemistry and Chemical Engineering, California Institute of Technology; Pasadena, 91125 CA, USA.
[14]CENTRA and Faculdade de Ciências da Universidade de Lisboa; 1749-016 Lisboa, Portugal.
[15]Research Center for Eco-Environmental Sciences, Chinese Academy of Sciences; 100084 Beijing, China.
[16]Helsinki Institute of Physics, University of Helsinki; 00014 Helsinki, Finland.
[17]Institute of Ion Physics and Applied Physics, University of Innsbruck; 6020 Innsbruck, Austria.
[18]Climate & Atmosphere Research Centre (CARE-C), The Cyprus Institute; 1645 Nicosia, Cyprus.
[19]Aerodyne Research, Inc.; 45 Manning Road, Billerica, 01821 MA, USA.
[20]Department of Chemical Engineering, Carnegie Mellon University; Pittsburgh, 15213 PA, USA.
[21]P.N. Lebedev Physical Institute of the Russian Academy of Sciences; 119991 Moscow, Russia.
[22]Moscow Institute of Physics and Technology (National Research University);141701 Moscow, Russian Federation.
[23]CERN, the European Organization for Nuclear Research; CH-1211 Geneva, Switzerland.
[24]Department of Physics, University of Genoa & INFN; 16146 Genoa, Italy.

[25]Department of Chemistry, Carnegie Mellon University, Pittsburgh, PA 15213, USA.
[26]Department of Atmospheric and Oceanic Sciences, University of Colorado, Boulder, CO 80309, USA.
[27]Natural environment research council, British Antarctic survey, CB3 0ET Cambridge, UK.
[28]Department of Chemistry, University of Helsinki, 00014 Helsinki, Finland.
[29]Department of Applied Physics, University of Eastern Finland, 70211 Kuopio, Finland.
[30]IDL-Universidade da Beira Interior, Rua Marquês D'Ávila e Bolama 6201-001 Covilhã, Portugal.
[31]University of Vienna, Faculty of Physics, Boltzmanngasse 5, 1090 Wien, Austria.
[32]Department of Engineering and Public Policy, Carnegie Mellon University, Pittsburgh, PA 15213, USA.
[33]Joint International Research Laboratory of Atmospheric and Earth System Sciences, School of Atmospheric Sciences, Nanjing University, 210023 Nanjing, China.
[34]Aerosol and Haze Laboratory, Beijing Advanced Innovation Center for Soft Matter Science and Engineering, Beijing University of Chemical Technology, Beijing 100029, China.

***Corresponding author.**

Xu-Cheng He (xucheng.he@helsinki.fi)

Markku Kulmala (markku.kulmala@helsinki.fi)

Mikko Sipilä (mikko.sipila@helsinki.fi)

Hong-Bin Xie (hbxie@dlut.edu.cn)

Abstract:

The main nucleating vapor in the atmosphere is thought to be sulfuric acid (H_2SO_4), stabilized by ammonia (NH_3). However, in marine and polar regions, NH_3 is generally low but H_2SO_4 is frequently found together with iodine oxoacids (HIO_x, i.e., iodic acid, HIO_3, and iodous acid, HIO_2). Here, in experiments performed with the CERN CLOUD chamber, we investigate the interplay of H_2SO_4 and HIO_x during atmospheric particle nucleation. We find that HIO_x greatly enhances H_2SO_4(-NH_3) nucleation, due to two interactions. First, HIO_3 strongly binds with H_2SO_4 in charged clusters so they drive particle nucleation synergistically. Second, HIO_2 substitutes for NH_3, forming strongly-bound H_2SO_4-HIO_2 acid-base pairs in molecular clusters. Global observations imply that HIO_x is enhancing H_2SO_4(-NH_3) nucleation rates by 10-10,000 times in marine and polar regions.

One-Sentence Summary:

Iodine oxoacids, sulfuric acid and ammonia drive particle nucleation synergistically in pristine marine and polar atmospheres.

Main Text:

Aerosols influence climate by acting as cloud condensation nuclei (CCN) and by scattering solar radiation. Secondary aerosol and cloud condensation nuclei formation continue to be two of the largest uncertainties hindering accurate projection of climate change(*1*). Only a few vapors in the atmosphere can nucleate to form new aerosol particles, which can further grow to CCN sizes. Sulfuric acid, H_2SO_4, is considered to be the primary vapor(*2*) driving particle formation in the atmosphere from polluted-(*3*, *4*) to pristine environments(*5–7*). However, as H_2SO_4-H_2O binary nucleation is slow, stabilizing vapors such as ammonia (NH_3), amines, and oxidized organics are generally needed to explain observed particle formation rates(*3–11*).

In terms of radiative balance, marine clouds, especially low-level marine stratocumulus(*12*), are key players since they have strong longwave emission and efficiently reflect solar radiation back to space. Since marine cloud formation is often limited by low CCN number concentrations, it is important to reach a comprehensive understanding of new particle formation in marine environments. New particle and subsequent CCN formation in marine regions is presently thought to be driven by H_2SO_4 and methanesulfonic acid (MSA)(*8*, *13*), aided by NH_3(*5*, *14*). However, a recent global survey of aerosol acidity suggests that global models substantially overestimate NH_3 concentrations; in particular, the polar atmosphere and high altitudes are characterized by low NH_3 concentrations(*15*). Assuming solely H_2SO_4 nucleation, advanced Earth system models struggle to reproduce aerosol number concentrations measured by aircraft(*16*), leading to low confidence for estimates of aerosol radiative forcing. Iodine-driven nucleation(*17–21*) has not yet been incorporated into Earth system models; iodine oxoacids (HIO_x, x = 2-3 in this study) can drive rapid particle formation under low NH_3 conditions, and they may play an important role in polar, marine and free tropospheric particle formation.

In the marine atmosphere, iodine and sulfur precursors emitted from the ocean surface lead to the formation of both H_2SO_4 and HIO_x(*22*). HIO_x has generally been observed at concentrations similar to or less than H_2SO_4(*6*, *18*, *21*, *23*). Despite the higher nucleation potential of HIO_x compared with H_2SO_4(*18*), iodine-driven new particle formation has hitherto been considered important only in regions with significantly higher concentrations of HIO_3 than of H_2SO_4, such as coastal zones and specific regions in the Arctic(*17*, *18*, *20*, *21*, *24*, *25*). However, new particle formation from the mixed chemical system, HIO_x-H_2SO_4(-NH_3), has not been reported so far.

Particle formation experiments in CLOUD

Here we report laboratory experiments performed in the CERN CLOUD (Cosmics Leaving Outdoor Droplets) chamber(*5*) (see Methods for details) between September 2018 and December 2019 under conditions relevant for marine and polar environments. We performed particle formation experiments involving HIO_x-H_2SO_4(-NH_3) vapors produced from the following precursors: molecular iodine (I_2), sulfur dioxide (SO_2), ammonia (NH_3), ozone (O_3) and water vapor (H_2O).

To investigate possible synergies in HIO_x-H_2SO_4(-NH_3) nucleation, green and ultraviolet light sources were used to drive photochemical production of HIO_x and H_2SO_4 from I_2 and SO_2. An example experiment at −10 °C is shown in Fig. 1 and Fig. S1, and at 10 °C in Fig. S2. Experiments were first performed without any added NH_3 (< 4 parts per trillion by volume, pptv contaminant level); these are shown in the left-hand panels of Fig. 1, S1 and S2. A second set of experiments was performed with NH_3 added to the chamber (right-hand panels of Fig. 1, S1 and S2). At both temperatures, significantly higher $J_{1.7}$ is observed in the presence of HIO_x than the $J_{1.7}$ expected from H_2SO_4-NH_3 nucleation (*5*, *14*), both without and with added NH_3.

In Fig. 2, we present nucleation rates at 1.7 nm, $J_{1.7}$, for the HIO_x-H_2SO_4 system (hollow markers) and the HIO_x-H_2SO_4-NH_3 system (filled markers) at 10 °C (circles) and −10 °C (squares). The concentration ranges of HIO_x and H_2SO_4 closely match ambient values, spanning from below 10^6 cm^{-3} to nearly 10^8 cm^{-3}(*6*, *17*, *18*, *20*, *21*, *23*). We show the measured $J_{1.7}$ for these mixed systems for various possible drivers: H_2SO_4 (Fig. 2A), HIO_3+H_2SO_4 (Fig. 2B) and (HIO_3 + H_2SO_4) × HIO_2 (Fig. 2C). The data at both temperatures become progressively less scattered when plotted against these variables, as well as more consistent with parameterizations(*14*, *18*). The H_2SO_4-NH_3 mechanism cannot predict the nucleation rates, even when the HIO_x concentration is much lower than H_2SO_4 (Fig. 2A). For instance, $J_{1.7}$ at 10 °C from HIO_x-H_2SO_4 with NH_3 < 4 pptv (hollow circles in Fig. 2A) is roughly 60 times faster than $J_{1.7}$ from H_2SO_4 with NH_3 at 4 pptv; this is as fast as nucleation from H_2SO_4 with NH_3 at 500 pptv. Therefore, sub-pptv levels of HIO_x are as effective at stabilizing H_2SO_4 as 500 pptv of NH_3. Hence, HIO_x may replace NH_3 as a nucleation driver in pristine marine and polar environments where NH_3 concentrations are typically below a few tens of pptv or below(*26*, *27*).

Fig. 2B shows the observed $J_{1.7}$ versus total acid concentration (HIO_3+H_2SO_4) and compares these rates to the values predicted by the H_2SO_4(-NH_3) parameterizations(*14*), applying (HIO_3+H_2SO_4) as H_2SO_4. The $J_{1.7}$ of the HIO_x-H_2SO_4 system without added NH_3 (open markers) remains higher than the prediction for H_2SO_4(-NH_3) nucleation. This indicates that HIO_x contributes more significantly to nucleation than simply increasing the acid concentration. Moreover, the relatively mild sensitivity to NH_3 suggests that the base stabilization comes from another source. This is supported by Fig. 2C, which indicates that HIO_2 is effectively providing base stabilization in the molecular clusters. To further investigate the underlying mechanisms, we studied the molecular composition of nucleating particles under neutral (ion-free) and charged (ion-induced) conditions, as described below.

HIO_2 accelerates neutral nucleation

To measure neutral clusters, we used a nitrate chemical ionization mass spectrometer (nitrate-CIMS). The concentrations of monomers, HIO_3, H_2SO_4, and iodous acid, HIO_2, are presented in Fig. 3A together with four product dimers in Fig. 3B. Although the HIO_2 concentration was 1-2 orders of magnitude below that of HIO_3 or H_2SO_4, the most prominent dimers, HIO_3-HIO_2 and H_2SO_4-HIO_2, both contain HIO_2. While HIO_3-HIO_2 clusters have been reported before(*18*, *28*), we believe this is the first observation of H_2SO_4-HIO_2 dimers.

While HIO_2 enables H_2SO_4-HIO_2 dimer formation, its role in larger clusters is not clear. We address this with a combination of quantum chemical calculations and cluster dynamics modelling(*29*). We optimized the geometries of H_2SO_4-HIO_2, HIO_3-HIO_2, and H_2SO_4-HIO_3-HIO_2 clusters and calculated their formation free energies and evaporation rates (Fig. S3). Clusters containing HIO_2 are the most stable and, moreover, show an exceptionally wide range stable combinations of molecules. The cluster geometries suggest that HIO_2 enhances H_2SO_4 neutral nucleation in the same way as it does for HIO_3 neutral nucleation(*18*). Specifically, HIO_2 accepts the proton donated either by H_2SO_4 or HIO_3, thereby functioning as a base. Furthermore, HIO_2 forms strong halogen bonds with H_2SO_4 and HIO_3, further enhancing the cluster stability. Cluster involving HIO_2 are even more stable than H_2SO_4-DMA (dimethyl amine) clusters (Fig. S3), which is known to cluster at the collision limit for sulfuric acid with only 4 pptv DMA(*3*). However, the predicted neutral nucleation rates for the H_2SO_4-HIO_2 and HIO_3-HIO_2 systems still under-estimate

our measured nucleation rates (GCR conditions, the sum of neutral and ion-induced channels) at −10 °C (orange band in Fig. 2C). On the other hand, the predicted HIO_x-H_2SO_4 neutral nucleation rates approximately agree CLOUD observations (squares and diamonds in Fig. 2C). The consistency between theoretical predictions and the CLOUD measurements at −10 °C suggests that neutral nucleation dominates at this temperature, which is also indicated since the nucleation rates far exceed the ion-pair production rate limit (2-10 cm^{-3} s^{-1}). Additionally, this suggests that the controlling mechanism is indeed a synergy of three molecules (HIO_3, H_2SO_4 and HIO_2) and not simply the combined neutral nucleation of any two molecules. Given that HIO_2 behaves as a base, we show in Fig. 2C our observed $J_{1.7}$ versus (HIO_3 + H_2SO_4) × HIO_2. This expression is proportional to the formation rate of the dimer (H_2SO_4-HIO_2 or HIO_3-HIO_2), which represents the initial nucleating cluster. We find that the HIO_x-H_2SO_4(-NH_3) nucleation rates fall near the prediction from HIO_x nucleation ($J_{1.7}$ vs. HIO_3 × HIO_2; H_2SO_4 is absent in pure iodine oxoacid nucleation)(*18*), implying that HIO_2 indeed plays the key role as stabilizer both for HIO_3 and H_2SO_4, NH_3 plays a minor role.

While the formation mechanism for HIO_3 has recently been established(*22*), the pathway for HIO_2 formation remains uncertain. A quantum chemical study provided a potential energy surface describing formation of HIO_2 from iodooxy hypoiodite, I_2O_2 + H_2O(*30*). We have extended this study with high-level quantum chemical calculations and provide a revised potential energy surface in Fig. S4. We also present a potential new pathway for HIO_2 formation from iodine dioxide, OIO and hydroperoxyl radical, HO_2 (Fig. S4B). Our calculations show that both the singlet and triplet channels are exothermic. Further studies are needed to quantify the relative importance in the atmosphere of these two channels.

Since complex reactions are involved in the formation of HIO_3 and HIO_2, it is important to confirm that the HIO_3:HIO_2 ratio in the CLOUD chamber matches ambient conditions. Fig. S5 shows that both the ratio and absolute concentrations of HIO_3 and HIO_2 fall within the range measured at Mace Head(*17*) and Ny-Ålesund(*21*), confirming that the results from our study are relevant to the atmosphere.

HIO_3 enhances ion-induced nucleation

Ions can stabilize embryonic molecular clusters, leading to ion-induced nucleation (IIN)(*5*, *18*, *19*, *31*, *32*). To investigate the influence of ions on HIO_x-H_2SO_4 nucleation, we increased the ionization rate in the chamber in three steps: i) neutral (ion-free), ii) galactic cosmic ray ionization (GCR, ca. 1000 ion pairs cm^{-3}) and iii) beam-enhanced ionization (ca. 6000 ion pairs cm^{-3}), at 10 °C (Fig. S6). Compared with neutral conditions, $J_{1.7}$ at GCR ionization rates is enhanced by ca. 50 times at 2×10^7 cm^{-3} H_2SO_4 and 5×10^6 cm^{-3} HIO_3. As with HIO_x, ion-induced HIO_x-H_2SO_4 nucleation only occurs with negative ions (Fig. S6A compared with Fig. S6B). Interestingly, six times larger ion concentrations formed by the pion beam only enhance $J_{1.7}$ by a factor of two. This is likely because the increased ion-ion recombination rate, and hence shorter charge lifetime, neutralizes some clusters before they have become stable against evaporation when neutral. When NH_3 is added to the HIO_x-H_2SO_4 system, it initiates positive IIN that is as strong as negative IIN at −10 °C (Fig. S1D). This approximately doubles the overall $J_{1.7}$.

To measure the molecular composition of charged clusters, we used an atmospheric pressure interface time-of-flight mass spectrometer. For HIO_x-H_2SO_4 IIN without NH_3 injection (Fig. 3C and 3D), we observe a series of charged clusters with the empirical formula, $(HIO_3)_n$-$(H_2SO_4)_m$-HSO_4^- (cyan triangles), which indicate synergistic IIN of HIO_3 and H_2SO_4. We identify these clusters as (n+m+1)-mer (which include the ion, Fig. S7). At 10 °C, monomers, dimers and trimers consist primarily of H_2SO_4, while HIO_3 appears in clusters starting from the tetramers and becomes equal to the H_2SO_4 mole fraction already in the hexamers. At −10 °C, HIO_3 appears in the dimers and becomes equal to the H_2SO_4 starting with the tetramers.

In this experiment, the HIO_3:H_2SO_4 ratio in the gas phase is between 0.3 and 1.4, and the molar ratios of I:S in the larger clusters tend towards 1:1, but with molecules containing iodine somewhat below those containing sulfur. We also know that pure ion-induced HIO_3 nucleation proceeds at the collision limit(*18*, *19*) but that ion-induced H_2SO_4 nucleation is slower than the collision limit(*5*). We therefore conclude that H_2SO_4 condensation is enhanced by HIO_3 for a cluster stoichiometry up to 1:1, beyond which the net rate of H_2SO_4 condensation slows, while HIO_3 condensation is limited by the collision rate under our experimental conditions.

We performed additional experiments in which NH_3 was added to the HIO_x-H_2SO_4 system. Interestingly, none of the charged pure iodine (i.e., H_2SO_4-free) clusters contains NH_3, which

indicates a negligible role of NH_3 in ion-induced HIO_3 nucleation. This was independently confirmed by raising NH_3 from the background level (< 4 pptv) to 100 pptv in an iodine oxoacid nucleation experiment without H_2SO_4 (Fig. S8). The measured nucleation rate at 1.7 nm, $J_{1.7}$, remained constant throughout the experiment, indicating that HIO_3(-HIO_2) nucleation is unaffected by NH_3.

On the other hand, we find a set of clusters with the composition $(H_2SO_4)_n$-$(NH_3)_m$-HSO_4^- and $(HIO_3)_n$-$(H_2SO_4)_m$-$(NH_3)_j$-HSO_4^- in the mass spectra of charged clusters (Fig. 3E and F), similar to the clusters reported near the coast of Antarctica(*6*). We find NH_3 is only present in charged tetramers and above, consistent with its behavior in H_2SO_4-NH_3 IIN(*5*). The iodine and sulfur molar fraction distributions remain unchanged after adding NH_3 to the system, likely because the HIO_3-H_2SO_4 negative IIN has already reached the collision limit (Fig. S7). The presence of NH_3 only converts some of the $(HIO_3)_n$-$(H_2SO_4)_m$-HSO_4^- to $(HIO_3)_n$-$(H_2SO_4)_m$-$(NH_3)_j$-HSO_4^- ions, and gives rise to positive IIN (Fig. S1).

Particle growth

Since the atmospheric concentration of HIO_2 is less than one-tenth that of HIO_3, its role in particle growth is minor(*18*). To evaluate the role of HIO_3 and H_2SO_4 in particle growth, we compare in Fig. S9A our measured growth rates between 1.8 and 3.2 nm ($GR_{1.8\text{-}3.2}$) with those calculated assuming condensation of H_2SO_4 and HIO_3(*18*, *33*) at the collision limit. The good agreement indicates that H_2SO_4 and HIO_3 are the main condensing vapors driving particle growth(*18*, *33*) while other iodine species contribute little to particle mass. We show in Fig. S9B the measured and predicted particle survival probability, $J_{2.5}/J_{1.7}$, which increases at faster growth rates and approaches unity above growth rates of ~10 nm h^{-1} for the CLOUD chamber (2.2×10^{-3} s^{-1} wall loss rate). In the marine atmosphere, condensation of other compounds such as methanesulfonic acid and oxidized organic molecules can also contribute to early particle growth, in addition to H_2SO_4 and HIO_3.

Climate implications

Atmospheric observations show that both iodine oxoacid and sulfuric acid-ammonia nucleation can be important particle sources in specific regions of the pristine boundary layer(*6*, *17*, *18*, *20*, *21*). So far, HIO_3 and HIO_2 have thought to be important only in regions where they are more

abundant than H_2SO_4. In polar and marine environments, it is currently thought that H_2SO_4-NH_3 constitutes the primary source of new particle formation, despite the perceived scarcity of NH_3(*15*). This picture is challenged by our findings. Instead, our data support the reverse: H_2SO_4-NH_3 nucleation plays a major role only when H_2SO_4 is substantially more abundant than HIO_3 and HIO_2. The role of HIO_x in atmospheric aerosol nucleation may have been overlooked as studies could easily be deceived by relatively higher H_2SO_4 than HIO_x in parts of the pristine atmosphere.

To assess the atmospheric importance of HIO_x-H_2SO_4(-NH_3) nucleation, we calculated the $J_{1.7}$ enhancement factor (the ratio of $J_{1.7}$ from HIO_x-H_2SO_4(-NH_3) to that from H_2SO_4-NH_3)(*14*) as a function of the HIO_3:H_2SO_4 concentration ratio (Fig. 4B). The enhancement factors are large, ranging from 10 to 10^4 for atmospherically-relevant HIO_3:H_2SO_4 ratios. Even when the HIO_3:H_2SO_4 ratio is 0.1, the enhancement factor is 10. Observations at marine and polar sites from the North Pole to Antarctica, show median HIO_3:H_2SO_4 ratios larger than 0.1 (Fig. 4A), implying that synergistic HIO_x-H_2SO_4(-NH_3) nucleation may have global importance, and yet has hitherto been overlooked. This conclusion is supported by our calculations of sulfuric acid nucleation enhanced by HIO_x, which are shown in Fig. S10. At −10 °C, which is representative of the marine free troposphere, fast nucleation rates of up to 10 cm^{-3} s^{-1} are estimated for ambient acid concentrations. The pronounced temperature dependence of HIO_x-H_2SO_4(-NH_3) nucleation that we find in our study may help explain why nucleation in the marine boundary is rarely observed, whereas nucleation is frequently found in the free troposphere or the upper marine boundary layer following passage of a cold front(*23*, *34*, *35*).

New particle formation from HIO_x-H_2SO_4 has notable implications for the future climate. Iodine oxoacids may enhance cloud condensation nuclei and cloud formation in the Arctic(*20*), which would, in turn, affect both longwave and shortwave radiative forcing at the surface(*36*). The absence of iodine oxoacid nucleation mechanisms in climate models may help explain why they systematically underestimate the CCN number concentration around the coast of Antarctica(*37*, *38*). Iodine has also been observed in both gas and particle phases in the polar and marine free troposphere and upper troposphere/lower stratosphere(*39*, *40*). These regions are characterized by low temperatures and extremely low NH_3 concentrations(*15*), which thus strongly favors HIO_x-H_2SO_4 or pure HIO_x nucleation over H_2SO_4-NH_3 nucleation. While global anthropogenic SO_2 emissions continue to fall due to emission policies, iodine emissions have tripled since the 1950s,

and this trend continues(*41*, *42*). As a result, nucleation mechanisms involving iodine oxoacids are anticipated to become even more important in future. To sharpen the understanding of marine aerosol-cloud radiative forcing, it is important that representations of new particle formation in global climate models now include iodine oxoacids together with sulfuric acid.

References and Notes

1. V. Masson-Delmotte, P. Zhai, A. Pirani, S. L. Connors, C. Péan, S. Berger, N. Caud, Y. Chen, L. Goldfarb, M. I. Gomis, M. Huang, K. Leitzell, E. Lonnoy, J. B. R. Matthews, T. K. Maycock, T. Waterfield, O. Yelekçi, R. Yu, B. Zhou, IPCC, 2021: Climate Change 2021: The Physical Science Basis. Contribution of Working Group I to the Sixth Assessment Report of the Intergovernmental Panel on Climate Change (Cambridge University Press., United Kingdom, 2021).

2. V.-M. Kerminen, X. Chen, V. Vakkari, T. Petäjä, M. Kulmala, F. Bianchi, Atmospheric new particle formation and growth: review of field observations. *Environmental Research Letters.* **13**, 103003 (2018).

3. J. Almeida, S. Schobesberger, A. Kürten, I. K. Ortega, O. Kupiainen-Määttä, A. P. Praplan, A. Adamov, A. Amorim, F. Bianchi, M. Breitenlechner, A. David, J. Dommen, N. M. Donahue, A. Downard, E. Dunne, J. Duplissy, S. Ehrhart, R. C. Flagan, A. Franchin, R. Guida, J. Hakala, A. Hansel, M. Heinritzi, H. Henschel, T. Jokinen, H. Junninen, M. Kajos, J. Kangasluoma, H. Keskinen, A. Kupc, T. Kurtén, A. N. Kvashin, A. Laaksonen, K. Lehtipalo, M. Leiminger, J. Leppä, V. Loukonen, V. Makhmutov, S. Mathot, M. J. McGrath, T. Nieminen, T. Olenius, A. Onnela, T. Petäjä, F. Riccobono, I. Riipinen, M. Rissanen, L. Rondo, T. Ruuskanen, F. D. Santos, N. Sarnela, S. Schallhart, R. Schnitzhofer, J. H. Seinfeld, M. Simon, M. Sipilä, Y. Stozhkov, F. Stratmann, A. Tomé, J. Tröstl, G. Tsagkogeorgas, P. Vaattovaara, Y. Viisanen, A. Virtanen, A. Vrtala, P. E. Wagner, E. Weingartner, H. Wex, C. Williamson, D. Wimmer, P. Ye, T. Yli-Juuti, K. S. Carslaw, M. Kulmala, J. Curtius, U. Baltensperger, D. R. Worsnop, H. Vehkamäki, J. Kirkby, Molecular understanding of sulphuric acid–amine particle nucleation in the atmosphere. *Nature*. **502**, 359–363 (2013).

4. M. Xiao, C. R. Hoyle, L. Dada, D. Stolzenburg, A. Kürten, M. Wang, H. Lamkaddam, O. Garmash, B. Mentler, U. Molteni, A. Baccarini, M. Simon, X.-C. He, K. Lehtipalo, L. R. Ahonen, R. Baalbaki, P. S. Bauer, L. Beck, D. Bell, F. Bianchi, S. Brilke, D. Chen, R. Chiu, A. Dias, J. Duplissy, H. Finkenzeller, H. Gordon, V. Hofbauer, C. Kim, T. K. Koenig, J. Lampilahti, C. P. Lee, Z. Li, H. Mai, V. Makhmutov, H. E. Manninen, R. Marten, S. Mathot, R. L. Mauldin, W. Nie, A. Onnela, E. Partoll, T. Petäjä, J. Pfeifer, V. Pospisilova, L. L. J. Quéléver, M. Rissanen, S. Schobesberger, S. Schuchmann, Y. Stozhkov, C. Tauber, Y. J. Tham, A. Tomé, M. Vazquez-Pufleau, A. C. Wagner, R. Wagner, Y. Wang, L. Weitz, D. Wimmer, Y. Wu, C. Yan, P. Ye, Q. Ye, Q. Zha, X. Zhou, A. Amorim, K. Carslaw, J. Curtius, A. Hansel, R. Volkamer, P. M. Winkler, R. C. Flagan, M. Kulmala, D. R. Worsnop, J. Kirkby, N. M. Donahue, U. Baltensperger, I. El Haddad, J. Dommen, The driving factors of new particle formation and growth in the polluted boundary layer. *Atmospheric Chemistry Physics.* **21**, 14275–14291 (2021).

5. J. Kirkby, J. Curtius, J. Almeida, E. Dunne, J. Duplissy, S. Ehrhart, A. Franchin, S. Gagné, L. Ickes, A. Kürten, A. Kupc, A. Metzger, F. Riccobono, L. Rondo, S. Schobesberger, G. Tsagkogeorgas, D. Wimmer, A. Amorim, F. Bianchi, M. Breitenlechner, A. David, J. Dommen, A. Downard, M. Ehn, R. C. Flagan, S. Haider, A. Hansel, D. Hauser, W. Jud, H. Junninen, F. Kreissl, A. Kvashin, A. Laaksonen, K. Lehtipalo, J. Lima, E. R. Lovejoy, V. Makhmutov, S. Mathot, J. Mikkilä, P. Minginette, S. Mogo, T. Nieminen, A. Onnela, P. Pereira, T. Petäjä, R. Schnitzhofer, J. H. Seinfeld, M. Sipilä, Y. Stozhkov, F. Stratmann, A. Tomé, J. Vanhanen, Y. Viisanen, A. Vrtala, P. E. Wagner, H. Walther, E. Weingartner, H.

Wex, P. M. Winkler, K. S. Carslaw, D. R. Worsnop, U. Baltensperger, M. Kulmala, Role of sulphuric acid, ammonia and galactic cosmic rays in atmospheric aerosol nucleation. *Nature*. **476**, 429–433 (2011).

6. T. Jokinen, M. Sipilä, J. Kontkanen, V. Vakkari, P. Tisler, E.-M. Duplissy, H. Junninen, J. Kangasluoma, H. E. Manninen, T. Petäjä, M. Kulmala, D. R. Worsnop, J. Kirkby, A. Virkkula, V.-M. Kerminen, Ion-induced sulfuric acid–ammonia nucleation drives particle formation in coastal Antarctica. *Science Advances*. **4**, eaat9744 (2018).

7. J. Brean, M. Dall'Osto, R. Simó, Z. Shi, D. C. S. Beddows, R. M. Harrison, Open ocean and coastal new particle formation from sulfuric acid and amines around the Antarctic Peninsula. *Nature Geoscience.* **14**, 383–388 (2021).

8. S. M. Kreidenweis, J. H. Seinfeld, Nucleation of sulfuric acid-water and methanesulfonic acid-water solution particles: implications for the atmospheric chemistry of organosulfur species. *Atmospheric Environment (1967)*. **22**, 283–296 (1988).

9. P. H. McMurry, Photochemical aerosol formation from SO_2: A theoretical analysis of smog chamber data. *Journal of Colloid and Interface Science*. **78**, 513–527 (1980).

10. C. Kuang, P. H. McMurry, A. V. McCormick, F. L. Eisele, Dependence of nucleation rates on sulfuric acid vapor concentration in diverse atmospheric locations. *Journal of Geophysical Research.* **113**, D10209 (2008).

11. C. Yan, R. Yin, Y. Lu, L. Dada, D. Yang, Y. Fu, J. Kontkanen, C. Deng, O. Garmash, J. Ruan, R. Baalbaki, M. Schervish, R. Cai, M. Bloss, T. Chan, T. Chen, Q. Chen, X. Chen, Y. Chen, B. Chu, K. Dällenbach, B. Foreback, X. He, L. Heikkinen, T. Jokinen, H. Junninen, J. Kangasluoma, T. Kokkonen, M. Kurppa, K. Lehtipalo, H. Li, H. Li, X. Li, Y. Liu, Q. Ma, P. Paasonen, P. Rantala, R. E. Pileci, A. Rusanen, N. Sarnela, P. Simonen, S. Wang, W. Wang, Y. Wang, M. Xue, G. Yang, L. Yao, Y. Zhou, J. Kujansuu, T. Petäjä, W. Nie, Y. Ma, M. Ge, H. He, N. M. Donahue, D. R. Worsnop, Veli‐Matti Kerminen, L. Wang, Y. Liu, J. Zheng, M. Kulmala, J. Jiang, F. Bianchi, The Synergistic Role of Sulfuric Acid, Bases, and Oxidized Organics Governing New‐Particle Formation in Beijing. *Geophysical Research Letters*. **48,** e2020GL091944 (2021).

12. R. Wood, Stratocumulus Clouds. *Monthly Weather Review*. **140**, 2373–2423 (2012).

13. M. L. Dawson, M. E. Varner, V. Perraud, M. J. Ezell, R. B. Gerber, B. J. Finlayson-Pitts, Simplified mechanism for new particle formation from methanesulfonic acid, amines, and water via experiments and ab initio calculations. *Proceedings of the National Academy of Sciences*. **109**, 18719–18724 (2012).

14. E. M. Dunne, H. Gordon, A. Kürten, J. Almeida, J. Duplissy, C. Williamson, I. K. Ortega, K. J. Pringle, A. Adamov, U. Baltensperger, P. Barmet, F. Benduhn, F. Bianchi, M. Breitenlechner, A. Clarke, J. Curtius, J. Dommen, N. M. Donahue, S. Ehrhart, R. C. Flagan, A. Franchin, R. Guida, J. Hakala, A. Hansel, M. Heinritzi, T. Jokinen, J. Kangasluoma, J. Kirkby, M. Kulmala, A. Kupc, M. J. Lawler, K. Lehtipalo, V. Makhmutov, G. Mann, S. Mathot, J. Merikanto, P. Miettinen, A. Nenes, A. Onnela, A. Rap, C. L. S. Reddington, F.

Riccobono, N. A. D. Richards, M. P. Rissanen, L. Rondo, N. Sarnela, S. Schobesberger, K. Sengupta, M. Simon, M. Sipilä, J. N. Smith, Y. Stozkhov, A. Tomé, J. Tröstl, P. E. Wagner, D. Wimmer, P. M. Winkler, D. R. Worsnop, K. S. Carslaw, Global atmospheric particle formation from CERN CLOUD measurements. *Science*. **354**, 1119–1124 (2016).

15. B. A. Nault, P. Campuzano-Jost, D. A. Day, D. S. Jo, J. C. Schroder, H. M. Allen, R. Bahreini, H. Bian, D. R. Blake, M. Chin, S. L. Clegg, P. R. Colarco, J. D. Crounse, M. J. Cubison, P. F. DeCarlo, J. E. Dibb, G. S. Diskin, A. Hodzic, W. Hu, J. M. Katich, M. J. Kim, J. K. Kodros, A. Kupc, F. D. Lopez-Hilfiker, E. A. Marais, A. M. Middlebrook, J. Andrew Neuman, J. B. Nowak, B. B. Palm, F. Paulot, J. R. Pierce, G. P. Schill, E. Scheuer, J. A. Thornton, K. Tsigaridis, P. O. Wennberg, C. J. Williamson, J. L. Jimenez, Chemical transport models often underestimate inorganic aerosol acidity in remote regions of the atmosphere. *Communications Earth and Environment*. **2**, 93 (2021).

16. A. Ranjithkumar, H. Gordon, C. Williamson, A. Rollins, K. Pringle, A. Kupc, N. L. Abraham, C. Brock, K. Carslaw, Constraints on global aerosol number concentration, SO_2 and condensation sink in UKESM1 using ATom measurements. *Atmospheric Chemistry and Physics.* **21**, 4979–5014 (2021).

17. M. Sipilä, N. Sarnela, T. Jokinen, H. Henschel, H. Junninen, J. Kontkanen, S. Richters, J. Kangasluoma, A. Franchin, O. Peräkylä, M. P. Rissanen, M. Ehn, H. Vehkamäki, T. Kurten, T. Berndt, T. Petäjä, D. Worsnop, D. Ceburnis, V.-M. Kerminen, M. Kulmala, C. O'Dowd, Molecular-scale evidence of aerosol particle formation via sequential addition of HIO_3. *Nature*. **537**, 532–534 (2016).

18. X.-C. He, Y. J. Tham, L. Dada, M. Wang, H. Finkenzeller, D. Stolzenburg, S. Iyer, M. Simon, A. Kürten, J. Shen, B. Rörup, M. Rissanen, S. Schobesberger, R. Baalbaki, D. S. Wang, T. K. Koenig, T. Jokinen, N. Sarnela, L. J. Beck, J. Almeida, S. Amanatidis, A. Amorim, F. Ataei, A. Baccarini, B. Bertozzi, F. Bianchi, S. Brilke, L. Caudillo, D. Chen, R. Chiu, B. Chu, A. Dias, A. Ding, J. Dommen, J. Duplissy, I. El Haddad, L. Gonzalez Carracedo, M. Granzin, A. Hansel, M. Heinritzi, V. Hofbauer, H. Junninen, J. Kangasluoma, D. Kemppainen, C. Kim, W. Kong, J. E. Krechmer, A. Kvashin, T. Laitinen, H. Lamkaddam, C. P. Lee, K. Lehtipalo, M. Leiminger, Z. Li, V. Makhmutov, H. E. Manninen, G. Marie, R. Marten, S. Mathot, R. L. Mauldin, B. Mentler, O. Möhler, T. Müller, W. Nie, A. Onnela, T. Petäjä, J. Pfeifer, M. Philippov, A. Ranjithkumar, A. Saiz-Lopez, I. Salma, W. Scholz, S. Schuchmann, B. Schulze, G. Steiner, Y. Stozhkov, C. Tauber, A. Tomé, R. C. Thakur, O. Väisänen, M. Vazquez-Pufleau, A. C. Wagner, Y. Wang, S. K. Weber, P. M. Winkler, Y. Wu, M. Xiao, C. Yan, Q. Ye, A. Ylisirniö, M. Zauner-Wieczorek, Q. Zha, P. Zhou, R. C. Flagan, J. Curtius, U. Baltensperger, M. Kulmala, V.-M. Kerminen, T. Kurtén, N. M. Donahue, R. Volkamer, J. Kirkby, D. R. Worsnop, M. Sipilä, Role of iodine oxoacids in atmospheric aerosol nucleation. *Science*. **371**, 589–595 (2021).

19. X.-C. He, S. Iyer, M. Sipilä, A. Ylisirniö, M. Peltola, J. Kontkanen, R. Baalbaki, M. Simon, A. Kürten, Y. J. Tham, J. Pesonen, L. R. Ahonen, S. Amanatidis, A. Amorim, A. Baccarini, L. Beck, F. Bianchi, S. Brilke, D. Chen, R. Chiu, J. Curtius, L. Dada, A. Dias, J. Dommen, N. M. Donahue, J. Duplissy, I. El Haddad, H. Finkenzeller, L. Fischer, M. Heinritzi, V. Hofbauer, J. Kangasluoma, C. Kim, T. K. Koenig, J. Kubečka, A. Kvashnin, H. Lamkaddam, C. P. Lee, M. Leiminger, Z. Li, V. Makhmutov, M. Xiao, R. Marten, W. Nie, A. Onnela, E.

Partoll, T. Petäjä, V.-T. Salo, S. Schuchmann, G. Steiner, D. Stolzenburg, Y. Stozhkov, C. Tauber, A. Tomé, O. Väisänen, M. Vazquez-Pufleau, R. Volkamer, A. C. Wagner, M. Wang, Y. Wang, D. Wimmer, P. M. Winkler, D. R. Worsnop, Y. Wu, C. Yan, Q. Ye, K. Lehtinen, T. Nieminen, H. E. Manninen, M. Rissanen, S. Schobesberger, K. Lehtipalo, U. Baltensperger, A. Hansel, V.-M. Kerminen, R. C. Flagan, J. Kirkby, T. Kurtén, M. Kulmala, Determination of the collision rate coefficient between charged iodic acid clusters and iodic acid using the appearance time method. *Aerosol Science and Technology*. **55**, 231–242 (2021).

20. A. Baccarini, L. Karlsson, J. Dommen, P. Duplessis, J. Vüllers, I. M. Brooks, A. Saiz-Lopez, M. Salter, M. Tjernström, U. Baltensperger, P. Zieger, J. Schmale, Frequent new particle formation over the high Arctic pack ice by enhanced iodine emissions. *Nature Communications*. **11**, 4924 (2020).

21. L. J. Beck, N. Sarnela, H. Junninen, C. J. M. Hoppe, O. Garmash, F. Bianchi, M. Riva, C. Rose, O. Peräkylä, D. Wimmer, O. Kausiala, T. Jokinen, L. Ahonen, J. Mikkilä, J. Hakala, X. He, J. Kontkanen, K. K. E. Wolf, D. Cappelletti, M. Mazzola, R. Traversi, C. Petroselli, A. P. Viola, V. Vitale, R. Lange, A. Massling, J. K. Nøjgaard, R. Krejci, L. Karlsson, P. Zieger, S. Jang, K. Lee, V. Vakkari, J. Lampilahti, R. C. Thakur, K. Leino, J. Kangasluoma, E. Duplissy, E. Siivola, M. Marbouti, Y. J. Tham, A. Saiz‐Lopez, T. Petäjä, M. Ehn, D. R. Worsnop, H. Skov, M. Kulmala, V. Kerminen, M. Sipilä, Differing Mechanisms of New Particle Formation at Two Arctic Sites. *Geophysical Research Letters*. **48,** e2020GL091334 (2021).

22. H. Finkenzeller, S. Iyer, X.-C. He, M. Simon, T. K. Koenig, C. F. Lee, R. Valiev, V. Hofbauer, A. Amorim, R. Baalbaki, A. Baccarini, L. Beck, D. M. Bell, L. Caudillo, D. Chen, R. Chiu, B. Chu, L. Dada, J. Duplissy, M. Heinritzi, D. Kemppainen, C. Kim, J. Krechmer, A. Kürten, A. Kvashnin, H. Lamkaddam, C. P. Lee, K. Lehtipalo, Z. Li, V. Makhmutov, H. E. Manninen, G. Marie, R. Marten, R. L. Mauldin, B. Mentler, T. Müller, T. Petäjä, M. Philippov, A. Ranjithkumar, B. Rörup, J. Shen, D. Stolzenburg, C. Tauber, Y. J. Tham, A. Tomé, M. Vazquez-Pufleau, A. C. Wagner, D. S. Wang, M. Wang, Y. Wang, S. K. Weber, W. Nie, Y. Wu, M. Xiao, Q. Ye, M. Zauner-Wieczorek, A. Hansel, U. Baltensperger, J. Brioude, J. Curtius, N. M. Donahue, I. E. Haddad, R. C. Flagan, M. Kulmala, J. Kirkby, M. Sipilä, D. R. Worsnop, T. Kurten, M. Rissanen, R. Volkamer, The gas-phase formation mechanism of iodic acid as an atmospheric aerosol source. *Nature Chemistry.* **15, 129-135** (2023).

23. A. Baccarini, J. Dommen, K. Lehtipalo, S. Henning, R. L. Modini, M. Gysel‐Beer, U. Baltensperger, J. Schmale, Low‐Volatility Vapors and New Particle Formation Over the Southern Ocean During the Antarctic Circumnavigation Expedition. *Journal of Geophysical Research: Atmosphere*. **126,** e2021JD035126 (2021).

24. T. Hoffmann, C. D. O'Dowd, J. H. Seinfeld, Iodine oxide homogeneous nucleation: An explanation for coastal new particle production. *Geophysical Research Letters*. **28**, 1949–1952 (2001).

25. C. D. O'Dowd, J. L. Jimenez, R. Bahreini, R. C. Flagan, J. H. Seinfeld, K. Hämeri, L. Pirjola, M. Kulmala, S. G. Jennings, T. Hoffmann, Marine aerosol formation from biogenic iodine emissions. *Nature*. **417**, 632–636 (2002).

26. G. R. Wentworth, J. G. Murphy, B. Croft, R. V. Martin, J. R. Pierce, J.-S. Côté, I. Courchesne, J.-É. Tremblay, J. Gagnon, J. L. Thomas, S. Sharma, D. Toom-Sauntry, A. Chivulescu, M. Levasseur, J. P. D. Abbatt, Ammonia in the summertime Arctic marine boundary layer: sources, sinks, and implications. *Atmospheric Chemistry Physics.* **16**, 1937–1953 (2016).

27. K. E. Altieri, K. A. M. Spence, S. Smith, Air‐Sea Ammonia Fluxes Calculated From High‐Resolution Summertime Observations Across the Atlantic Southern Ocean. *Geophysical Research Letters*. **48,** e2020GL091963 (2021).

28. R. Zhang, H.-B. Xie, F. Ma, J. Chen, S. Iyer, M. Simon, M. Heinritzi, J. Shen, Y. J. Tham, T. Kurtén, D. R. Worsnop, J. Kirkby, J. Curtius, M. Sipilä, M. Kulmala, X.-C. He, Critical Role of Iodous Acid in Neutral Iodine Oxoacid Nucleation. *Environmental Science and Technology*. **56**, 14166-14177 (2022).

29. M. J. McGrath, T. Olenius, I. K. Ortega, V. Loukonen, P. Paasonen, T. Kurtén, M. Kulmala, H. Vehkamäki, Atmospheric Cluster Dynamics Code: a flexible method for solution of the birth-death equations. *Atmospheric Chemistry Physics.* **12**, 2345–2355 (2012).

30. J. C. Gómez Martín, T. R. Lewis, M. A. Blitz, J. M. C. Plane, M. Kumar, J. S. Francisco, A. Saiz-Lopez, A gas-to-particle conversion mechanism helps to explain atmospheric particle formation through clustering of iodine oxides. *Nature Communications*. **11**, 4521 (2020).

31. S.-H. Lee, J. M. Reeves, J. C. Wilson, D. E. Hunton, A. A. Viggiano, T. M. Miller, J. O. Ballenthin, L. R. Lait, Particle Formation by Ion Nucleation in the Upper Troposphere and Lower Stratosphere. *Science*. **301**, 1886–1889 (2003).

32. E. R. Lovejoy, Atmospheric ion-induced nucleation of sulfuric acid and water. *Journal of Geophysical Research*. **109,** D0820 (2004).

33. D. Stolzenburg, M. Simon, A. Ranjithkumar, A. Kürten, K. Lehtipalo, H. Gordon, S. Ehrhart, H. Finkenzeller, L. Pichelstorfer, T. Nieminen, X.-C. He, S. Brilke, M. Xiao, A. Amorim, R. Baalbaki, A. Baccarini, L. Beck, S. Bräkling, L. Caudillo Murillo, D. Chen, B. Chu, L. Dada, A. Dias, J. Dommen, J. Duplissy, I. El Haddad, L. Fischer, L. Gonzalez Carracedo, M. Heinritzi, C. Kim, T. K. Koenig, W. Kong, H. Lamkaddam, C. P. Lee, M. Leiminger, Z. Li, V. Makhmutov, H. E. Manninen, G. Marie, R. Marten, T. Müller, W. Nie, E. Partoll, T. Petäjä, J. Pfeifer, M. Philippov, M. P. Rissanen, B. Rörup, S. Schobesberger, S. Schuchmann, J. Shen, M. Sipilä, G. Steiner, Y. Stozhkov, C. Tauber, Y. J. Tham, A. Tomé, M. Vazquez-Pufleau, A. C. Wagner, M. Wang, Y. Wang, S. K. Weber, D. Wimmer, P. J. Wlasits, Y. Wu, Q. Ye, M. Zauner-Wieczorek, U. Baltensperger, K. S. Carslaw, J. Curtius, N. M. Donahue, R. C. Flagan, A. Hansel, M. Kulmala, J. Lelieveld, R. Volkamer, J. Kirkby, P. M. Winkler, Enhanced growth rate of atmospheric particles from sulfuric acid. *Atmospheric Chemistry Physics.* **20**, 7359–7372 (2020).

34. K. J. Sanchez, G. C. Roberts, G. Saliba, L. M. Russell, C. Twohy, J. M. Reeves, R. S. Humphries, M. D. Keywood, J. P. Ward, I. M. McRobert, Measurement report: Cloud processes and the transport of biological emissions affect southern ocean particle and cloud condensation nuclei concentrations. *Atmospheric Chemistry Physics.* **21**, 3427–3446 (2021).

35. G. Zheng, Y. Wang, R. Wood, M. P. Jensen, C. Kuang, I. L. McCoy, A. Matthews, F. Mei, J. M. Tomlinson, J. E. Shilling, M. A. Zawadowicz, E. Crosbie, R. Moore, L. Ziemba, M. O. Andreae, J. Wang, New particle formation in the remote marine boundary layer. *Nature Communications*. **12**, 527 (2021).

36. T. Mauritsen, J. Sedlar, M. Tjernström, C. Leck, M. Martin, M. Shupe, S. Sjogren, B. Sierau, P. O. G. Persson, I. M. Brooks, E. Swietlicki, An Arctic CCN-limited cloud-aerosol regime. *Atmospheric Chemistry Physics.* **11**, 165–173 (2011).

37. I. L. McCoy, D. T. McCoy, R. Wood, L. Regayre, D. Watson-Parris, D. P. Grosvenor, J. P. Mulcahy, Y. Hu, F. A.-M. Bender, P. R. Field, K. S. Carslaw, H. Gordon, The hemispheric contrast in cloud microphysical properties constrains aerosol forcing. *Proceedings of the National Academy of Sciences*. **117**, 18998–19006 (2020).

38. L. A. Regayre, J. Schmale, J. S. Johnson, C. Tatzelt, A. Baccarini, S. Henning, M. Yoshioka, F. Stratmann, M. Gysel-Beer, D. P. Grosvenor, K. S. Carslaw, The value of remote marine aerosol measurements for constraining radiative forcing uncertainty. *Atmospheric Chemistry Physics.* **20**, 10063–10072 (2020).

39. R. Volkamer, S. Baidar, T. L. Campos, S. Coburn, J. P. DiGangi, B. Dix, E. W. Eloranta, T. K. Koenig, B. Morley, I. Ortega, B. R. Pierce, M. Reeves, R. Sinreich, S. Wang, M. A. Zondlo, P. A. Romashkin, Aircraft measurements of BrO, IO, glyoxal, NO_2, H_2O, O_2-O_2 and aerosol extinction profiles in the tropics: Comparison with aircraft-/ship-based in situ and lidar measurements. *Atmospheric Measurement Techniques*. **8**, 2121–2148 (2015).

40. T. K. Koenig, S. Baidar, P. Campuzano-Jost, C. A. Cuevas, B. Dix, R. P. Fernandez, H. Guo, S. R. Hall, D. Kinnison, B. A. Nault, K. Ullmann, J. L. Jimenez, A. Saiz-Lopez, R. Volkamer, Quantitative detection of iodine in the stratosphere. *Proceedings of the National Academy of Sciences*. **114**, 1860-1866 (2020).

41. C. A. Cuevas, N. Maffezzoli, J. P. Corella, A. Spolaor, P. Vallelonga, H. A. Kjær, M. Simonsen, M. Winstrup, B. Vinther, C. Horvat, R. P. Fernandez, D. Kinnison, J.-F. Lamarque, C. Barbante, A. Saiz-Lopez, Rapid increase in atmospheric iodine levels in the North Atlantic since the mid-20th century. *Nature Communications*. **9**, 1452 (2018).

42. M. Legrand, J. R. McConnell, S. Preunkert, M. Arienzo, N. Chellman, K. Gleason, T. Sherwen, M. J. Evans, L. J. Carpenter, Alpine ice evidence of a three-fold increase in atmospheric iodine deposition since 1950 in Europe due to increasing oceanic emissions. *Proceedings of the National Academy of Sciences*. **115**, 12136–12141 (2018).

43. X.-C. He, M. Simon, S. Iyer, H.-B. Xie, B. Rörup, J. Shen, H. Finkenzeller, D. Stolzenburg, R. Zhang, A. Baccarini, Y. J. Tham, M. Wang, S. Amanatidis, A. A. Piedehierro, A. Amorim, R. Baalbaki, Z. Brasseur, L. Caudillo, B. Chu, L. Dada, J. Duplissy, I. El Haddad, R. C. Flagan, M. Granzin, A. Hansel, M. Heinritzi, V. Hofbauer, T. Jokinen, D. Kemppainen, W. Kong, J. Krechmer, A. Kürten, H. Lamkaddam, B. Lopez, F. Ma, N. G. A. Mahfouz, V. Makhmutov, H. E. Manninen, G. Marie, R. Marten, D. Massabò, R. L. Mauldin, B. Mentler, A. Onnela, T. Petäjä, J. Pfeifer, M. Philippov, A. Ranjithkumar, M. P. Rissanen, S. Schobesberger, W. Scholz, B. Schulze, M. Surdu, R. C. Thakur, A. Tomé, A. C. Wagner, D. Wang, S. K. Weber, A. Welti, P. M. Winkler, M. Zauner-Wieczorek, U. Baltensperger, J.

Curtius, T. Kurtén, D. R. Worsnop, R. Volkamer, K. Lehtipalo, J. Kirkby, N. M. Donahue, M. Sipilä, M. Kulmala, Iodine oxoacids enhance nucleation of sulfuric acid particles in the atmosphere: data resources, Version 1, Zenodo (2023); https://zenodo.org/record/8344386.

44. A. Dias, S. Ehrhart, A. Vogel, C. Williamson, J. Almeida, J. Kirkby, S. Mathot, S. Mumford, A. Onnela, Temperature uniformity in the CERN CLOUD chamber. *Atmospheric Measurement Techniques.* **10**, 5075–5088 (2017).

45. J. Duplissy, J. Merikanto, A. Franchin, G. Tsagkogeorgas, J. Kangasluoma, D. Wimmer, H. Vuollekoski, S. Schobesberger, K. Lehtipalo, R. C. Flagan, D. Brus, N. M. Donahue, H. Vehkamäki, J. Almeida, A. Amorim, P. Barmet, F. Bianchi, M. Breitenlechner, E. M. Dunne, R. Guida, H. Henschel, H. Junninen, J. Kirkby, A. Kürten, A. Kupc, A. Määttänen, V. Makhmutov, S. Mathot, T. Nieminen, A. Onnela, A. P. Praplan, F. Riccobono, L. Rondo, G. Steiner, A. Tome, H. Walther, U. Baltensperger, K. S. Carslaw, J. Dommen, A. Hansel, T. Petäjä, M. Sipilä, F. Stratmann, A. Vrtala, P. E. Wagner, D. R. Worsnop, J. Curtius, M. Kulmala, Effect of ions on sulfuric acid-water binary particle formation: 2. Experimental data and comparison with QC-normalized classical nucleation theory. *Journal of Geophysical Research: Atmospheres*. **121**, 1752–1775 (2016).

46. H. Junninen, M. Ehn, T. Petäjä, L. Luosujärvi, T. Kotiaho, R. Kostiainen, U. Rohner, M. Gonin, K. Fuhrer, M. Kulmala, D. R. Worsnop, A high-resolution mass spectrometer to measure atmospheric ion composition. *Atmospheric Measurement Techniques*. **3**, 1039–1053 (2010).

47. M. P. Rissanen, J. Mikkilä, S. Iyer, J. Hakala, Multi-scheme chemical ionization inlet (MION) for fast switching of reagent ion chemistry in atmospheric pressure chemical ionization mass spectrometry (CIMS) applications. *Atmospheric Meassurement Techniques.* **12**, 6635–6646 (2019).

48. H. E. Manninen, S. Mirme, A. Mirme, T. Petäjä, M. Kulmala, How to reliably detect molecular clusters and nucleation mode particles with Neutral cluster and Air Ion Spectrometer (NAIS). *Atmospheric Meassurement Techniques.* **9**, 3577–3605 (2016).

49. S. Mirme, A. Mirme, The mathematical principles and design of the NAIS – a spectrometer for the measurement of cluster ion and nanometer aerosol size distributions. *Atmospheric Meassurement Techniques.* **6**, 1061–1071 (2013).

50. J. Vanhanen, J. Mikkilä, K. Lehtipalo, M. Sipilä, H. E. Manninen, E. Siivola, T. Petäjä, M. Kulmala, Particle Size Magnifier for Nano-CN Detection. *Aerosol Science and Technology*. **45**, 533–542 (2011).

51. J. Tröstl, T. Tritscher, O. F. Bischof, H.-G. Horn, T. Krinke, U. Baltensperger, M. Gysel, Fast and precise measurement in the sub-20nm size range using a Scanning Mobility Particle Sizer. *Journal of Aerosol Science*. **87**, 75–87 (2015).

52. D. Stolzenburg, G. Steiner, P. M. Winkler, A DMA-train for precision measurement of sub-10 nm aerosol dynamics. *Atmospheric Meassurement Techniques.* **10**, 1639–1651 (2017).

53. M. Wang, X.-C. He, H. Finkenzeller, S. Iyer, D. Chen, J. Shen, M. Simon, V. Hofbauer, J. Kirkby, J. Curtius, N. Maier, T. Kurtén, D. R. Worsnop, M. Kulmala, M. Rissanen, R.

Volkamer, Y. J. Tham, N. M. Donahue, M. Sipilä, Measurement of iodine species and sulfuric acid using bromide chemical ionization mass spectrometers. *Atmospheric Meassurement Techniques.* **14**, 4187–4202 (2021).

54. J. Pfeifer, M. Simon, M. Heinritzi, F. Piel, L. Weitz, D. Wang, M. Granzin, T. Müller, S. Bräkling, J. Kirkby, J. Curtius, A. Kürten, Measurement of ammonia, amines and iodine compounds using protonated water cluster chemical ionization mass spectrometry. *Atmospheric Measurement Techniques*. **13**, 2501–2522 (2020).

55. M. Breitenlechner, L. Fischer, M. Hainer, M. Heinritzi, J. Curtius, A. Hansel, PTR3: An Instrument for Studying the Lifecycle of Reactive Organic Carbon in the Atmosphere. *Analytical Chemistry.* **89**, 5824–5831 (2017).

56. M. Wang, M. Xiao, B. Bertozzi, G. Marie, B. Rörup, B. Schulze, R. Bardakov, X.-C. He, J. Shen, W. Scholz, R. Marten, L. Dada, R. Baalbaki, B. Lopez, H. Lamkaddam, H. E. Manninen, A. Amorim, F. Ataei, P. Bogert, Z. Brasseur, L. Caudillo, L.-P. De Menezes, J. Duplissy, A. M. L. Ekman, H. Finkenzeller, L. G. Carracedo, M. Granzin, R. Guida, M. Heinritzi, V. Hofbauer, K. Höhler, K. Korhonen, J. E. Krechmer, A. Kürten, K. Lehtipalo, N. G. A. Mahfouz, V. Makhmutov, D. Massabò, S. Mathot, R. L. Mauldin, B. Mentler, T. Müller, A. Onnela, T. Petäjä, M. Philippov, A. A. Piedehierro, A. Pozzer, A. Ranjithkumar, M. Schervish, S. Schobesberger, M. Simon, Y. Stozhkov, A. Tomé, N. S. Umo, F. Vogel, R. Wagner, D. S. Wang, S. K. Weber, A. Welti, Y. Wu, M. Zauner-Wieczorek, M. Sipilä, P. M. Winkler, A. Hansel, U. Baltensperger, M. Kulmala, R. C. Flagan, J. Curtius, I. Riipinen, H. Gordon, J. Lelieveld, I. El-Haddad, R. Volkamer, D. R. Worsnop, T. Christoudias, J. Kirkby, O. Möhler, N. M. Donahue, Synergistic HNO_3–H_2SO_4–NH_3 upper tropospheric particle formation. *Nature*. **605**, 483–489 (2022).

57. T. Jokinen, M. Sipilä, H. Junninen, M. Ehn, G. Lönn, J. Hakala, T. Petäjä, R. L. Mauldin, M. Kulmala, D. R. Worsnop, Atmospheric sulphuric acid and neutral cluster measurements using CI-APi-TOF. *Atmospheric Chemistry and Physics*. **12**, 4117–4125 (2012).

58. A. Kürten, T. Jokinen, M. Simon, M. Sipilä, N. Sarnela, H. Junninen, A. Adamov, J. Almeida, A. Amorim, F. Bianchi, M. Breitenlechner, J. Dommen, N. M. Donahue, J. Duplissy, S. Ehrhart, R. C. Flagan, A. Franchin, J. Hakala, A. Hansel, M. Heinritzi, M. Hutterli, J. Kangasluoma, J. Kirkby, A. Laaksonen, K. Lehtipalo, M. Leiminger, V. Makhmutov, S. Mathot, A. Onnela, T. Petäjä, A. P. Praplan, F. Riccobono, M. P. Rissanen, L. Rondo, S. Schobesberger, J. H. Seinfeld, G. Steiner, A. Tomé, J. Tröstl, P. M. Winkler, C. Williamson, D. Wimmer, P. Ye, U. Baltensperger, K. S. Carslaw, M. Kulmala, D. R. Worsnop, J. Curtius, Neutral molecular cluster formation of sulfuric acid–dimethylamine observed in real time under atmospheric conditions. *Proceedings of the National Academy of Sciences*. **111**, 15019–15024 (2014).

59. A. Kürten, L. Rondo, S. Ehrhart, J. Curtius, Calibration of a Chemical Ionization Mass Spectrometer for the Measurement of Gaseous Sulfuric Acid. *Journal of Physical Chemistry A*. **116**, 6375–6386 (2012).

60. B. K. Ku, J. F. de la Mora, Relation between Electrical Mobility, Mass, and Size for Nanodrops 1–6.5 nm in Diameter in Air. *Aerosol Science and Technology*. **43**, 241–249 (2009).

61. L. Dada, K. Lehtipalo, J. Kontkanen, T. Nieminen, R. Baalbaki, L. Ahonen, J. Duplissy, C. Yan, B. Chu, T. Petäjä, K. Lehtinen, V.-M. Kerminen, M. Kulmala, J. Kangasluoma, Formation and growth of sub-3-nm aerosol particles in experimental chambers. *Nature Protocols*. **15**, 1013–1040 (2020).

62. K. Lehtipalo, J. Leppa, J. Kontkanen, J. Kangasluoma, A. Franchin, D. Wimnner, S. Schobesberger, H. Junninen, T. Petaja, M. Sipila, others, Methods for determining particle size distribution and growth rates between 1 and 3 nm using the Particle Size Magnifier. *Boreal Environment Research*. **19**, 215–236 (2014).

63. V.-M. Kerminen, M. Kulmala, Analytical formulae connecting the "real" and the "apparent" nucleation rate and the nuclei number concentration for atmospheric nucleation events. *Journal of Aerosol Science*. **33**, 609–622 (2002).

64. K. E. J. Lehtinen, M. Dal Maso, M. Kulmala, V.-M. Kerminen, Estimating nucleation rates from apparent particle formation rates and vice versa: Revised formulation of the Kerminen–Kulmala equation. *Journal of Aerosol Science*. **38**, 988–994 (2007).

65. R. C. Thakur, L. Dada, L. J. Beck, L. L. J. Quéléver, T. Chan, M. Marbouti, X.-C. He, C. Xavier, J. Sulo, J. Lampilahti, M. Lampimäki, Y. J. Tham, N. Sarnela, K. Lehtipalo, A. Norkko, M. Kulmala, M. Sipilä, T. Jokinen, An evaluation of new particle formation events in Helsinki during a Baltic Sea cyanobacterial summer bloom. *Atmospheric Chemistry Physics.* **22**, 6365–6391 (2022).

66. T. Jokinen, K. Lehtipalo, R. C. Thakur, I. Ylivinkka, K. Neitola, N. Sarnela, T. Laitinen, M. Kulmala, T. Petäjä, M. Sipilä, Measurement report: Long-term measurements of aerosol precursor concentrations in the Finnish subarctic boreal forest. *Atmospheric Chemistry Physics.* **22**, 2237–2254 (2022).

67. H. Finkenzeller, S. Iyer, X.-C. He, M. Simon, T. K. Koenig, C. F. Lee, R. Valiev, V. Hofbauer, A. Amorim, R. Baalbaki, A. Baccarini, L. Beck, D. M. Bell, L. Caudillo, D. Chen, R. Chiu, B. Chu, L. Dada, J. Duplissy, M. Heinritzi, D. Kemppainen, C. Kim, J. Krechmer, A. Kürten, A. Kvashnin, H. Lamkaddam, C. P. Lee, K. Lehtipalo, Z. Li, V. Makhmutov, H. E. Manninen, G. Marie, R. Marten, R. L. Mauldin, B. Mentler, T. Müller, T. Petäjä, M. Philippov, A. Ranjithkumar, B. Rörup, J. Shen, D. Stolzenburg, C. Tauber, Y. J. Tham, A. Tomé, M. Vazquez-Pufleau, A. C. Wagner, D. S. Wang, M. Wang, Y. Wang, S. K. Weber, W. Nie, Y. Wu, M. Xiao, Q. Ye, M. Zauner-Wieczorek, A. Hansel, U. Baltensperger, J. Brioude, J. Curtius, N. M. Donahue, I. E. Haddad, R. C. Flagan, M. Kulmala, J. Kirkby, M. Sipilä, D. R. Worsnop, T. Kurten, M. Rissanen, R. Volkamer, The gas-phase formation mechanism of iodic acid as an atmospheric aerosol source. *Nature Chemistry.* **15**, 129–135 (2023).

68. H.-B. Xie, J. Elm, R. Halonen, N. Myllys, T. Kurtén, M. Kulmala, H. Vehkamäki, Atmospheric Fate of Monoethanolamine: Enhancing New Particle Formation of Sulfuric Acid as an Important Removal Process. *Environmental Science Technology.* **51**, 8422–8431 (2017).

69. J. Shen, H.-B. Xie, J. Elm, F. Ma, J. Chen, H. Vehkamäki, Methanesulfonic Acid-driven New Particle Formation Enhanced by Monoethanolamine: A Computational Study. *Environmental Science Technology.* **53**, 14387–14397 (2019).

70. R. Zhang, J. Shen, H.-B. Xie, J. Chen, J. Elm, The role of organic acids in new particle formation from methanesulfonic acid and methylamine. *Atmospheric Chemistry Physics.* **22**, 2639–2650 (2022).

71. I. Funes-Ardoiz, R. S. Paton, Goodvibes: Goodvibes V1.0.1 (2016), (available at https://zenodo.org/record/60811).

72. M. J. Frisch, G. W. Trucks, H. B. Schlegel, G. E. Scuseria, M. A. Robb, J. R. Cheeseman, G. Scalmani, V. Barone, G. A. Petersson, H. Nakatsuji, X. Li, M. Caricato, A. V. Marenich, J. Bloino, B. G. Janesko, R. Gomperts, B. Mennucci, H. P. Hratchian, J. V. Ortiz, A. F. Izmaylov, J. L. Sonnenberg, Williams, F. Ding, F. Lipparini, F. Egidi, J. Goings, B. Peng, A. Petrone, T. Henderson, D. Ranasinghe, V. G. Zakrzewski, J. Gao, N. Rega, G. Zheng, W. Liang, M. Hada, M. Ehara, K. Toyota, R. Fukuda, J. Hasegawa, M. Ishida, T. Nakajima, Y. Honda, O. Kitao, H. Nakai, T. Vreven, K. Throssell, J. A. Montgomery Jr., J. E. Peralta, F. Ogliaro, M. J. Bearpark, J. J. Heyd, E. N. Brothers, K. N. Kudin, V. N. Staroverov, T. A. Keith, R. Kobayashi, J. Normand, K. Raghavachari, A. P. Rendell, J. C. Burant, S. S. Iyengar, J. Tomasi, M. Cossi, J. M. Millam, M. Klene, C. Adamo, R. Cammi, J. W. Ochterski, R. L. Martin, K. Morokuma, O. Farkas, J. B. Foresman, D. J. Fox, Gaussian 16 Rev. C.01 (2016).

73. F. Neese, The ORCA program system: The ORCA program system. *Wiley Interdisciplinary Reviews: Computational Molecular Science*. **2**, 73–78 (2012).

74. R. Halonen, E. Zapadinsky, T. Kurtén, H. Vehkamäki, B. Reischl, Rate enhancement in collisions of sulfuric acid molecules due to long-range intermolecular forces. *Atmospheric Chemistry Physics.* **19**, 13355–13366 (2019).

75. F. Neese, F. Wennmohs, U. Becker, C. Riplinger, The ORCA quantum chemistry program package. *Journal of Chemical Physics.* **152**, 224108 (2020).

76. D. Feller, The role of databases in support of computational chemistry calculations. *Journal of Computational Chemistry*. **17**, 1571–1586 (1996).

77. K. A. Peterson, D. Figgen, E. Goll, H. Stoll, M. Dolg, Systematically convergent basis sets with relativistic pseudopotentials. II. Small-core pseudopotentials and correlation consistent basis sets for the post- *d* group 16–18 elements. *Journal of Chemical Physics*. **119**, 11113–11123 (2003).

Acknowledgments: We thank CERN for supporting CLOUD with important technical and financial resources, and for providing a particle beam from the CERN Proton Synchrotron. We thank the CSC IT Center for Science in Espoo, Finland, for computing time.

Funding:

Research Council of Finland ACCC Flagship no. 337549 and 337552.

Research Council of Finland professorship (302958).

Research Council of Finland Centre of Excellence no. 346371, 346372, 346373.

Research Council of Finland projects no. 335844, 334514, 346371, 345125, 325656, 316114, 314798, 325647, 353836, 341349 and 349659.

European Research Council (ERC) project no. 742206, 714621, 616075 and 101002728.

The Marie Sklodowska-Curie grant agreement no. 316662, 701647, 895875 and 764991.

National Natural Science Foundation of China no. 42175118 and 22236004.

National Key Research and Development Program of China (2022YFC3701000, Task 1).

Swiss National Science Foundation no. 200021_169090, 206021_198140, 200020_172602 and 20FI20_172622.

US National Science Foundation Grants no. AGS2132089, AGS1801897, AGS1801574, AGS-1801280, AGS-2027252, AGS-2215522, AGS-1602086, AGS-1801329 and AGS-2215527.

R.C.T. and M.K. thank Jane and Aatos Erkko Foundation for fundings.

M.K. received funding from Prince Albert Foundation Contract no. 2859.

Portuguese Science Foundation project CERN/FIS-COM/0028/2019.

M.W. thanks the Schmidt Science Fellowship for support.

X.-C.H. and M.K. thank Jenny and Antti Wihuri Foundation for funding.

Author contributions:

X.-C.H., J.Kir., M.Sip. and M.K. planned the experiments.

X.-C.H., M.Sim., B.R., J.S., H.F., D.S., A.B., Y.J.T., M.W., S.A., A.A.P., A.A., R.B., Z.B., L.C., B.C., L.D., J.D., I.E.-H., R.C.F., M.G., M.H., V.H., W.K., J.Kre, A.K., H.L., B.L., N.G.A.M., V.M., H.E.M., G.M., R.M., D.M., R.LM., B.M., A.O., T.P., J.P., M.P., M.P.R., S.S., W.S., B.S., M.S., A.T., A.C.W., D.W., Y.W., S.K.W., A.W., P.M.W., M.Z.-W., J.Kir, U.B., K.L., J.C., R.V., M.Sip. and M.K. prepared the CLOUD facility or measuring instruments.

X.-C.H., M.Sim., S.I., B.R., J.S., H.F., D.S., A.B., Y.J.T., A.A., R.B., L.C., L.D., J.D., I.E.-H., M.G., M.H., V.H., T.J., D.K., W.K., J.Kre, H.L., B.L., N.G.A.M., V.M., H.E.M., G.M., R.M., D.M., R.LM., B.M., J.P., A.R., W.S., R.C.T., A.C.W., D.W., S.K.W., M.Z.-W., J.Kir, J.C. and R.V. collected the data. X.-C.H., S.I., H.-B.X., H.F., D.S., R.Z., Y.J.T., L.C., L.D., R.C.F., F.M., W.S., R.C.T., S.K.W., P.M.W., T.K. and D.R.W. analysed the data.

X.-C.H., N.M.D. and J.Kir. wrote the manuscript with contributions from S.I., H.-B.X., B.R. and R.Z.

X.-C.H., M.Sim., S.I., H.-B.X., B.R., J.S., H.F., D.S., R.Z., A.B., L.D., J.D., I.E.-H., R.C.F., A.H., H.L., N.G.A.M., T.P., S.S., W.S., R.C.T., A.C.W., J.Kir, U.B., K.L., J.C., T.K., D.R.W., R.V., N.M.D., M.Sip. and M.K. commented on and edited the manuscript.

Competing interests: Authors declare that they have no competing interests.

Data and materials availability: Supplemental information is available for this paper. Data for all figures in the main text and supplementary materials are available at the Zenodo repository(*43*). Correspondence and additional requests for materials should be addressed to Xu-Cheng He (email: xucheng.he@helsinki.fi; permanent email: xuchenghe93@gmail.com).

Supplementary Materials

Materials and Methods

Figs. S1 to S10

References (*44–77*)

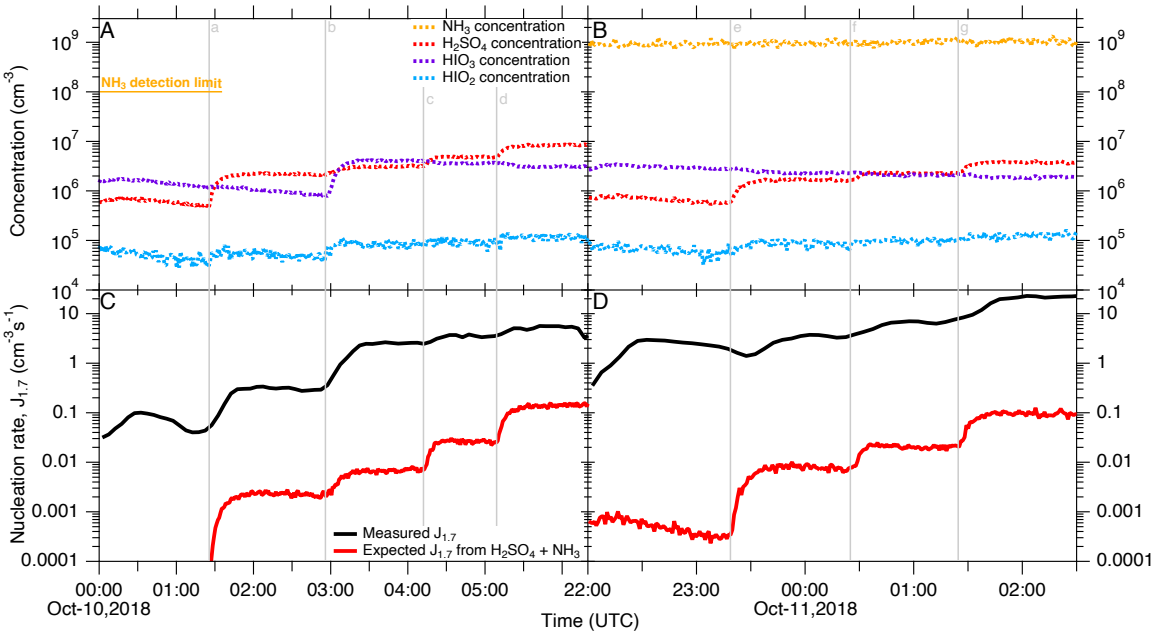

Fig. 1. New particle formation from HIO_x-H_2SO_4 (A, C) and HIO_x-H_2SO_4-NH_3 (B, D) at −10 °C. (A, B) vapor concentrations and (C, D) nucleation rates. Solid black lines show the measured nucleation rates at 1.7 nm, $J_{1.7}$ and solid red lines present predicted $J_{1.7}$ from H_2SO_4-NH_3 nucleation alone*(14)*. Dashed lines represent vapor concentrations and vertical grey bars show experimental stages. The experiments show that the rapid nucleation rates cannot be explained by the H_2SO_4-NH_3 mechanism alone. HIO_x significantly enhances H_2SO_4-NH_3 nucleation at comparable HIO_3 and H_2SO_4 concentrations. The NH_3 concentration in panel A is below the detection limit of the H_3O^+-CIMS (ca. 4 pptv). An NH_3 concentration of 4 pptv is used to conservatively estimate the H_2SO_4-NH_3 nucleation rates in panel C. The experimental conditions are 41.1 ppbv O_3, 63.5% RH, 2.3 ppbv SO_2 and 17.4 pptv I_2 (A, C), and 40.8 ppbv O_3, 62.3% RH, 1.6 ppbv SO_2 and 67.2 pptv I_2 (B, D). Stages (a, c, d, e, f, g) enhanced the UVH light intensity (higher OH production rates) and stage (b) increased the green light intensity (higher I_2 photolysis rate).

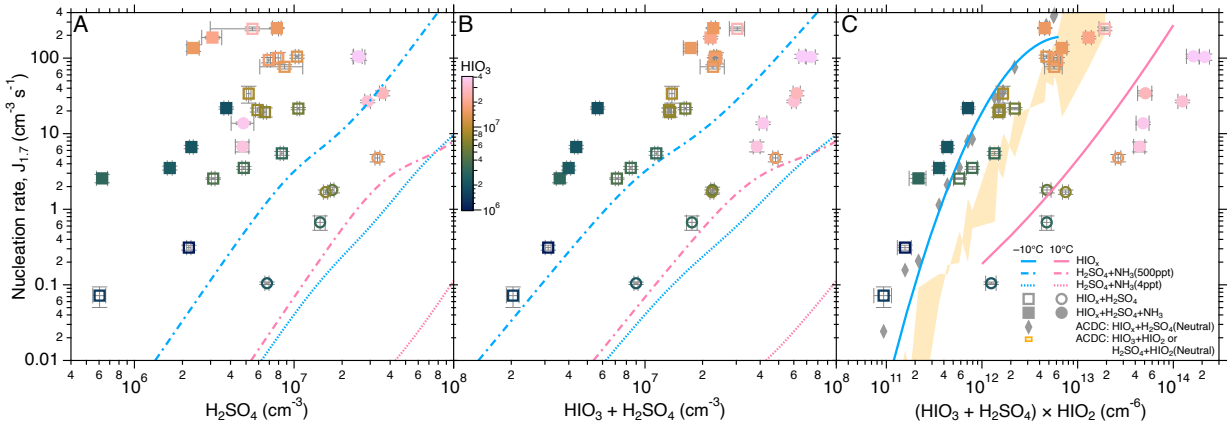

Fig. 2. Nucleation rates of HIO_x-H_2SO_4(-NH_3) systems. Nucleation rates at 1.7 nm, $J_{1.7}$ versus (A) H_2SO_4 (B) HIO_3 + H_2SO_4 and (C) (HIO_3 + H_2SO_4) × HIO_2 at +10 °C and −10 °C. All data points and lines show experiments carried out at galactic cosmic ray ionization conditions except for the ACDC simulations in panel C (orange band) which represent the theoretical prediction for the neutral nucleation rates (see Methods). The color bar represents HIO_3 concentration (cm^{-3}). H_2SO_4-NH_3 mechanism fails to predict the overall nucleation rates, even with HIO_x is much lower than H_2SO_4. The $J_{1.7}$ from experiments with high H_2SO_4 is also higher than that predicted by pure iodine oxoacids(*18*). The nucleation rates become less spread when plotted against (HIO_3 + H_2SO_4) × HIO_2, as well as more consistent with parameterizations and ACDC predictions. The results show that HIO_3 and HIO_2 have to be considered together with H_2SO_4 to predict the nucleation rates in this multi-component system. H_2SO_4-NH_3 nucleation rates (dotted and dash-dotted lines) are calculated based on Dunne et al.(*14*) while HIO_x nucleation rates (solid lines) are calculated based on $J_{1.7}$, HIO_3 and recalculated HIO_2 from He et al.(18), applying HIO_3 × HIO_2 as (HIO_3 + H_2SO_4) × HIO_2, to guide the eye. The experimental conditions for HIO_x-H_2SO_4(-NH_3) experiments are 38.4-53.2 ppbv O_3, 41.9-75.3 % RH, 0.6-11.2 ppbv SO_2 and 10.0-57.7 pptv I_2. The NH_3 concentrations for the filled squares and filled circles range from 30 to 42 pptv and from 176 to 261 pptv, respectively. The error bars show one standard deviation during the data selection periods. Overall systematic scale errors on the HIO_3 concentrations of −33% and +50% and on the nucleation rates of a factor of ten are not shown on the data points.

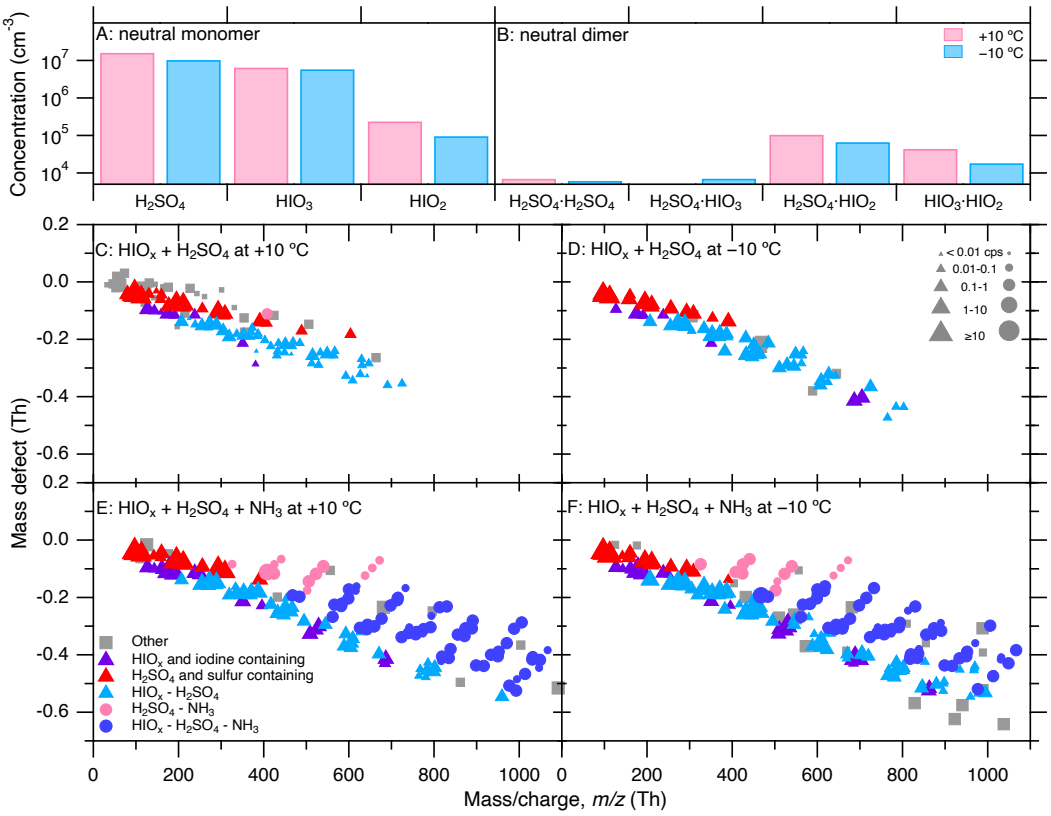

Fig. 3. Neutral and charged cluster composition during HIO_x-H_2SO_4-NH_3 nucleation. Background-subtracted neutral monomer (A) and dimer (B) concentrations in HIO_x-H_2SO_4 nucleation events at +10 °C (pink bars) and −10 °C (cyan bars). (C) and (D) show negatively-charged cluster compositions of HIO_x-H_2SO_4 nucleation at +10 °C and −10 °C, respectively. (E) and (F) show negatively charged cluster compositions of HIO_x-H_2SO_4-NH_3 nucleation at +10 °C and −10 °C, respectively. Panel B shows that the dominant neutral dimers are H_2SO_4-HIO_2 and HIO_3-HIO_2 clusters – despite very low HIO_2 concentrations – which represent the initial molecular clusters during neutral nucleation. Ion-induced nucleation is dominated by charged HIO_3-H_2SO_4 (C, D) or HIO_3-H_2SO_4(-NH_3) (E, F) cluster formation processes. HIO_3-NH_3 clusters are not detected which suggests that NH_3 has a negligible effect on ion-induced HIO_3 cluster formation. The marker size is shown in the legend (cps: ion counts per second). The experimental conditions are 38.5-43.9 ppbv O_3, 61.6-75.2% RH, 0.7-11.0 ppbv SO_2 and 14.4-44.5 pptv I_2.

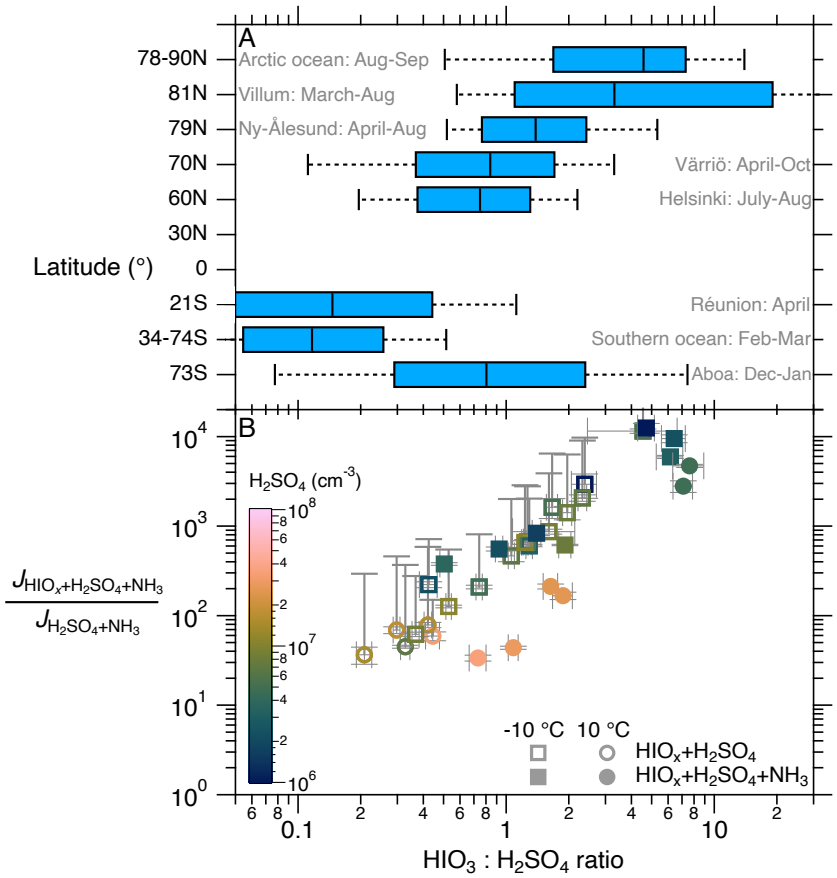

Fig. 4. HIO_x enhancement of H_2SO_4-NH_3 nucleation. (A) Box plot statistics of HIO_3:H_2SO_4 ratios measured around the globe, showing median values with 10% and 90% percentiles in the whiskers. The texts show the site name and months, with data covering more than 50% of the days. (B) Nucleation enhancement by HIO_x is calculated by dividing the measured $J_{HIO_x-H_2SO_4-NH_3}$ to predicte $J_{H_2SO_4-NH_3}$ using CLOUD parameterizations(*14*). The median ratios at all sites are greater than 0.1 which infers at least a 10 times nucleation rate enhancement by HIO_x. The enhancement is especially pronounced in polar regions where HIO_3:H_2SO_4 ratio is consistently higher than 0.1. Thin symmetric error bars represent one standard deviation during the data selection periods. In the experiments without NH_3 injection (hollow markers), the NH_3 concentrations were below the instrument detection limit (4 pptv) which is adopted as a conservative estimate of $J_{H_2SO_4-NH_3}$. However, the actual NH_3 concentration is expected to be below 1 pptv as all charged clusters are essentially NH_3 free (Fig. 3). The thick asymmetric error bars represent the systematic uncertainty assuming NH_3 equals 1 pptv. The NH_3 concentrations in experiments with NH_3 injection (filled markers) are well measured thus without asymmetric errors. The field observation sites are summarized in Methods.

Science
AAAS

Supplementary Materials for

Iodine oxoacids enhance nucleation of sulfuric acid particles in the atmosphere

Xu-Cheng He[1,2,3*], Mario Simon[4], Siddharth Iyer[5], Hong-Bin Xie[6*], Birte Rörup[1], Jiali Shen[1], Henning Finkenzeller[7,8], Dominik Stolzenburg[1,9], Rongjie Zhang[6], Andrea Baccarini[10,11], Yee Jun Tham[1,12], Mingyi Wang[13], Stavros Amanatidis[13], Ana A. Piedehierro[3], Antonio Amorim[14], Rima Baalbaki[1], Zoé Brasseur[1], Lucía Caudillo[4], Biwu Chu[1,15], Lubna Dada[1,10], Jonathan Duplissy[1,16], Imad El Haddad[10], Richard C Flagan[13], Manuel Granzin[4], Armin Hansel[17], Martin Heinritzi[4], Victoria Hofbauer[2], Tuija Jokinen[1,18], Deniz Kemppainen[1], Weimeng Kong[13], Jordan Krechmer[19], Andreas Kürten[4], Houssni Lamkaddam[10], Brandon Lopez[2,20], Fangfang Ma[6], Naser G. A. Mahfouz[2], Vladimir Makhmutov[21,22], Hanna E. Manninen[23], Guillaume Marie[4], Ruby Marten[10], Dario Massabò[24], Roy L. Mauldin[25,26], Bernhard Mentler[17], Antti Onnela[23], Tuukka Petäjä[1], Joschka Pfeifer[23], Maxim Philippov[21], Ananth Ranjithkumar[27], Matti P. Rissanen[5,28], Siegfried Schobesberger[29], Wiebke Scholz[17], Benjamin Schulze[13], Mihnea Surdu[10], Roseline C. Thakur[1], António Tomé[30], Andrea C. Wagner[4], Dongyu Wang[10], Yonghong Wang[1,15], Stefan K. Weber[23,4], André Welti[3], Paul M. Winkler[31], Marcel Zauner-Wieczorek[4], Urs Baltensperger[10], Joachim Curtius[4], Theo Kurtén[28], Douglas R. Worsnop[1,19], Rainer Volkamer[7,8], Katrianne Lehtipalo[1,3], Jasper Kirkby[23,4], Neil M. Donahue[2,20,25,32], Mikko Sipilä[1*], Markku Kulmala[1,16,33,34*]

Corresponding author: xucheng.he@helsinki.fi (X.-C.H.), markku.kulmala@helsinki.fi (M.K.), mikko.sipila@helsinki.fi (M.Sip.), hbxie@dlut.edu.cn (H.-B.X.)

The PDF file includes:

Materials and Methods

The CLOUD experiments

The experiments presented in this study were conducted in the CERN CLOUD (Cosmics Leaving OUtdoor Droplets) chamber, an electropolished, stainless-steel, 26.1 m^3 chamber which allows studying new particle formation under the full range of tropospheric and lower-stratospheric conditions. The thermal housing around the chamber is able to control the temperature from 208 to 373 K with high precision (± 0.1 K)(*44*). Ultra-pure synthetic air is derived from mixing cryogenic liquids (21% oxygen and 79% nitrogen) and is continuously injected into the chamber ensuring scrupulous cleanliness and minimal contamination(*5*, *45*). CLOUD deploys various light sources to drive photochemistry selectively. Hydroxyl radical production is initiated by illuminating O_3 with an ultra-violet fiber-optic system (UVH), including four 200 W Hamamatsu Hg-Xe lamps with a wavelength between 250 and 450 nm or a KrF excimer UV laser at 248 nm, both with adjustable powers. A green light saber centered at 528 nm is used to photolyze molecular iodine (I_2). All light systems are continuously monitored by a spectrometer and an array of photodiodes at the bottom of the chamber. Dedicated actinometry experiments allow quantitative determination of actinic fluxes of the light system at different intensities.

Particle formation under different ionization conditions is simulated by combining a strong electric field (± 30 kV) which eliminates natural ions in under 1 second, and the pion beam produced by CERN Proton Synchrotron which enhances ion production. Two magnetically coupled stainless-steel fans mounted at the top and bottom of the chamber enable uniform spatial mixing of particles and vapors within a few minutes. The chamber is characterized by a low loss rate (e.g., 0.0022 s^{-1} for sulfuric acid, H_2SO_4) which is comparable to the condensation sink values observed in pristine environments. The chamber is cleaned by rinsing the chamber walls with ultra-pure water and heating to 373 K for over 24 h between different experimental programs to avoid cross-contamination and to ensure extremely low NH_3 levels. I_2 in the chamber was sourced from crystalline iodine (I_2, Sigma-Aldrich, 99.999% purity) in a temperature-controlled evaporator, and was injected at the bottom of CLOUD. The SO_2 was injected into the chamber from a pressurized gas cylinder (CARBAGAS, AG, 100 ppm in N_2) and NH_3 was provided by a pressurized gas cylinder containing 1% NH_3 in N_2 (CARBAGAS, AG).

The results reported in this study were obtained from two CLOUD campaigns: 1) the CLOUD13 campaign from September to November 2018 and 2) the CLOUD14 campaign from September to November 2019. All the experiments at −10 °C (squares in Fig. 2) and HIO_x-H_2SO_4 (iodic acid, HIO_3; iodous acid, HIO_2 and sulfuric acid, H_2SO_4) experiments at 10 °C (hollow circles in Fig. 2) were carried out during CLOUD13. Repeated HIO_x experiments (larger hollow triangles), HIO_x-NH_3 experiments (filled triangles) and HIO_x-H_2SO_4-NH_3 experiments (filled circles) at 10 °C were carried out during CLOUD14. Repeated standard experiments such as photochemical production of H_2SO_4 and alpha-pinene ozonolysis experiments were carried out prior to physical experiments to ensure data consistency among different campaigns.

Instrumentation

Naturally charged clusters were measured with two atmospheric pressure interface time-of-flight mass spectrometer (APi-TOF, Aerodyne Inc.) operating at negative ion mode(*46*). The first APi-TOF was equipped with a multi-scheme chemical ionization inlet(*47*) (MION) operating at the APi-TOF mode (Fig. 3C, D). The second APi-TOF was coupled with an ion-molecule reaction chamber and a regular stainless-steel inlet into the chamber (Fig. 3E, F). Charged particle size distribution and mobilities both in negative and positive polarities were measured with a neutral cluster and air ion spectrometer (NAIS)(*48*, *49*) in the size range of 0.8 to 42 nm. Particle number size distribution between 1 and 3 nm was measured by nano-condensation nucleus counter (nCNC), consisting of a particle size magnifier (PSM, Airmodus Oy) coupled to a condensation particle counter (CPC). The PSM is an aerosol pre-conditioner, which uses diethylene glycol to grow aerosol particles as small as 1 nm to sizes that are easily detectable by a CPC(*50*). An additional butanol CPC (TSI 3776) was utilized to measure the total number concentration of particles with diameters larger than 2.5 nm.

The particle size distribution between 6 and 65 nm was measured by a nano scanning mobility particle sizer (TSI 3938)(*51*) and the particles bigger than 65 nm were measured by a custom-built long SMPS. In parallel, a differential mobility analyzer – train (DMA-train)(*52*) consisting of 6 DMAs measured the particle number size distribution between 1.8 and 8 nm, from which growth

rates in the size ranges 1.8-3.2 nm and 3.2-8 nm were retrieved with high precision. With these instruments, the particle size distribution from 1 nm to 1 μm is measured.

Gas monitors were used to measure sulfur dioxide (SO_2, Thermo Fisher Scientific Inc. 42i-TLE) and ozone (O_3 Thermo Environmental Instruments TEI 49C) and a cavity-enhanced differential optical absorption spectrometer (CE-DOAS) was used to measure molecular iodine, I_2. I_2 was additionally measured by a bromide chemical ionization mass spectrometer coupled with a multi-scheme chemical ionization inlet (Br^--MION-CIMS)(*47*, *53*) and was calibrated at CLOUD13 by comparing the measured normalized I_2 signal from Br^--MION-CIMS to the absolute value measured by the CE-DOAS(*53*). Ammonia (NH_3) was measured by H_3O^+-CIMS at CLOUD13 with a detection limit of 4 pptv at 278 K and 80 % RH(*54*). For a conservative calculation of the enhancement of HIO_x on H_2SO_4-NH_3 nucleation in this study, we assume the chamber NH_3 background equals 4 pptv at CLOUD13. However, it is worth noting that the actual NH_3 concentration in the chamber is very likely below 1 pptv, as evident from the fact that few of the charged clusters contain NH_3 in experiments without active NH_3 injection (Fig. 3C, D). In CLOUD14, a proton transfer reaction mass spectrometer 3 (PTR3)(*55*) was used to measure NH_3 as the H_3O^+-CIMS was not available. The PTR3 had a significantly higher NH_3 background due to the NH_3 – inlet wall interaction and an NH_3-collecting Teflon ball valve placed in between the instrument and the CLOUD chamber(*56*). The Teflon piece was needed as the PTR3 was regularly calibrated against standard volatile organic compounds during the experiments. In order to ensure NH_3-free initial conditions ($NH_3 < 1$ pptv), we alternatively used the APi-TOF as a qualitative NH_3 detector. The APi-TOF has been proven to be an extremely sensitive NH_3 detector once H_2SO_4 is present in the chamber as they form charged clusters efficiently(*5*). Therefore, prior to the experiments presented in this study from CLOUD14, H_2SO_4 nucleation experiments were carried out and we only found a few charged clusters containing NH_3, indicating the chamber was essentially NH_3 free. Additionally, the chamber was roasted at 100 °C for over 12 h to ensure removing any NH_3 wall residue. Despite the high NH_3 background, the PTR3 was still sensitive to the NH_3 changes in the chamber(*56*) and the final NH_3 values reported from CLOUD14 were background corrected by values before the NH_3 injection.

Sulfuric acid (H_2SO_4), iodic acid (HIO_3), iodous acid (HIO_2) and neutral dimers were measured with a nitrate chemical ionization mass spectrometer (NO_3^--CIMS). A NO_3^--CIMS is an APi-TOF coupled with a chemical ionization inlet that utilizes nitric acid (HNO_3) as the reagent gas to charge analytes in samples(*57*). An ion-filter was installed before the chemical ionization source to avoid interferences from naturally charged ions from the chamber. The details of the chemical ionization inlet used to measure the reported data points in this study can be found in our earlier study(*58*). The quantification of these acids follows a standard calibration method as described in Kürten et al. 2012(*59*).

Given the extensive research on H_2SO_4 and HIO_3 detection, and the fact that both are measured at the collision limit, we assess the efficiency of HIO_2 detection by combining experimental and theoretical evidence in this study. In our experiments, HIO_2 is primarily detected as HIO_2-HNO_3-NO_3^- (comprising 95%) using the NO_3^--CIMS. Our calculations (see details in quantum chemical calculations part) indicate that the preferred dissociation channel yields HIO_2-NO_3^- and HNO_3 as the products, with a formation enthalpy of 35.5 kcal mol^{-1}, thereby preserving the chemical signal of HIO_2. It is essential to note that a secondary dissociation channel forms HIO_2 and HNO_3-NO_3^- as the products and therefore causes the chemical signal of HIO_2 to be lost, owing to a slightly higher enthalpy of 35.7 kcal mol^{-1}. Since the preferred dissociation channel accounts for only 5% of total HIO_2 signals in the form of HIO_2-NO_3^-, we anticipate that the secondary dissociation channel leads to less than a 5% loss in the total HIO_2 signal. Consequently, HIO_2 is detected nearly at the collision limit.

Additionally, an independently calibrated NO_3^--CIMS-2 with a different inlet design(*57*) was used to cross-check the concentrations reported by the NO_3^--CIMS in CLOUD12. During the CLOUD13, the Br^--MION-CIMS was used to validate the reported acid concentrations. In both campaigns, the differences were within the reported systematic error of −33%/+50%. The data points reported in CLOUD14 were primarily provided by the NO_3^--CIMS (calibrated) as the NO_3^--CIMS-2 was absent. However, we note that the reported results from CLOUD14 (larger triangles and filled circles) are consistent with those reported from CLOUD12 and CLOUD13.

Calculation of the nucleation, growth rates and particle survival probability

The nucleation rate, $J_{1.7}$, is calculated at the 1.7 nm mobility diameter (1.4 nm in physical diameter(*60*)). Particles at 1.7 nm are commonly considered to be larger than their critical cluster sizes, and are therefore stable. In the absence of other particle sources than particle nucleation, the formation rates can be calculated from the time evolution of the particle concentration, taking into account the different loss processes that also affect the concentration. Since the loss processes in a chamber are different from those in the atmosphere, the method needs to be adjusted for chamber experiments(*61*). For the calculation of the formation rate (J_{dp}), we need to consider the losses specific to the CLOUD chamber, including dilution, wall and coagulation losses. In our case, it is calculated as below:

$$J_{\mathrm{dp}} = \frac{\mathrm{d}N}{\mathrm{d}t} + S_{\mathrm{dil}} + S_{\mathrm{wall}} + S_{\mathrm{coag}}$$

Where dN/dt is the time derivative of the total particle concentration above a certain particle size (here >1.7 nm for $J_{1.7}$ and >2.5 nm for $J_{2.5}$) and S_{dil}, S_{wall} and S_{coag} are the size-dependent particle losses due to dilution, wall and coagulation.

The particle growth rates are calculated using the 50% appearance time method as described in Dada et al.(*61*) and Lehtipalo et al.(*62*) and the theoretical derivation of the 50% appearance time method at the molecular level is provided in He et al.(*19*). Growth rates between 1.8 and 3.2 nm are derived from the DMA-train data(*52*).

The particle survival probability(*63*) in this study is defined as the probability of particles growing from 1.7 nm to 2.5 nm (both in mobility diameter) calculated by dividing the $J_{2.5}$ by the $J_{1.7}$ which both include the size-dependent losses to dilution, to the wall and to coagulation. The theoretical survival probability is calculated using Lehtinen et al.(*64*), an updated version of Kerminen and Kulmala equation(*63*).

Field observations

The acid concentrations from the Arctic Ocean were adopted from the MOCCHA campaign on board the Swedish I/B Oden in August and September 2018 as part of the Arctic Ocean expedition 2018(*20*). The campaign was especially characterized by over four weeks of ice-drift operation at latitudes higher than 88 °N, thus providing valuable information from the center of the Arctic Ocean.

The Villum research station is located in the northeast of Greenland. It is on Prinsesse Ingeborg Halvø peninsula. The data reported in this study is cited from a field observation carried out in March-August, 2015(*17*).

The Ny-Ålesund acid concentrations were measured at the Gruvebadet Observatory located at about 50 meters above sea level, 800 meters southwest of the village of Ny-Ålesund. The experiments were carried out between mid-February 2015 (data reported in this study starting from March 2015) until the end of August 2015(*21*).

The field observation at Helsinki was carried out between June and August 2018 during the summertime blooms in the Baltic Sea. The site is surrounded by forests, coastal waterbodies and a major road connecting the city center and suburban areas(*65*).

The Värriö research station is located in the north part of Finland. Measurements were done on top of Kotovaara hill (390 meters a.s.l.). The measurement period of reported data was from April to October 2019(*66*).

Réunion Island is located in the southwestern part of the Indian Ocean. The observation site was a modern research station on top of an old volcanic caldera (Maïdo-OPAR observatory, L'observatoire de physique de l'atmosphère de La Réunion). The site is located at 2160 m above sea level and is regularly exposed to free tropospheric air masses. The data reported in this study were obtained in April 2018(*22*).

The Antarctic Circumnavigation Expedition (ACE) was carried out between December 2016 (data reported in this study starting from January 2017) to March 2017 on board the Russian icebreaker Akademik Tryoshnikov(*23*). The expedition sailed around Antarctica and across the Southern Ocean, providing rare information on atmospheric trace gases.

The Finnish Antarctic research station (Aboa) is located on Basen Nunatak at Vestfjella mountains in Queen Maud Land, Eastern Antarctica. The measurement site is roughly 480 meters above sea level and 130 km south of the sea ice. The data reported in this study were obtained from December 2014 to January 2015(*6*).

Quantum chemical calculations and kinetics modeling

We investigated cluster formation of the binary HIO_3-HIO_2, H_2SO_4-HIO_2 and the ternary H_2SO_4-HIO_3-HIO_2 systems by employing quantum chemical calculations and kinetics modeling. Similar to previous studies(*67–69*), the global minimum structures of $(H_2SO_4)_{1\text{-}3}(HIO_2)_{1\text{-}3}$ and $(H_2SO_4)_x(HIO_3)_y(HIO_2)_z$ ($2 \leq x + y \leq 3$, z = 1-3) clusters were identified using a multistep global minimum sampling scheme. The geometries of pure $(H_2SO_4)_{1\text{-}3}$ and $(HIO_3)_{0\text{-}3}(HIO_2)_{0\text{-}3}$ were taken from our previous studies(*28, 67*). Briefly, around 5000-9000 initial configurations for each cluster were randomly generated, and then underwent a stepwise screening process with a series of theoretical methods to find the configuration with the lowest Gibbs free energy. The employed theoretical methods for configuration optimization and single-point energy calculations include PM7, M06-2X/def2-TZVP, M06-2X/aug-cc-pVTZ(-PP) and DLPNO-CCSD(T)/aug-cc-pVTZ(-PP) (aug-cc-pVTZ-PP for I atoms and aug-cc-pVTZ for H, O, S atoms). The GoodVibes program(*70*) was employed to recalculate the Gibbs free energy correction term (via quasi-harmonic correction) of clusters at the M06-2X/aug-cc-pVTZ(-PP) level with a low frequency cutoff value of 100 cm^{-1}. Finally, the conformer with the lowest Gibbs free energy at 298.15 K (the sum of single point energies at the DLPNO-CCSD(T)/aug-cc-pVTZ(-PP) level and the recalculated Gibbs free energy correction terms by GoodVibes) was determined as the global minimum for a given cluster. Additionally, we have obtained Gibbs free energies for all the global minima at other temperatures by combining the single point energies at the DLPNO-CCSD(T)/aug-cc-pVTZ(-PP) level and the recalculated Gibbs free energy correction terms by GoodVibes at corresponding temperature. Geometry optimization, frequency, and single-point

energy calculations using the PM7 and M06-2X methods were performed in the Gaussian 16 program(*71*) and DLPNO-CCSD(T)/aug-cc-pVTZ(-PP) calculations were performed using ORCA 4.0.0 program(*72*) with tight SCF and PNO convergence criteria. The formation free energy (ΔG) values for individual clusters were obtained by subtracting the sum of Gibbs free energies of their constituent molecules from that of the clusters at the considered temperature.

The atmospheric cluster dynamics code (ACDC)(*29*) was employed to simulate cluster formation rates for the comparison with CLOUD experiments. Here, the ACDC simulation system was performed on $(H_2SO_4)_x(HIO_3)_y(HIO_2)_z$ ($0 \leq x+y \leq 3$, z = 0-3) clusters. The $(H_2SO_4)_4(HIO_2)_4$, $(H_2SO_4)_3(HIO_2)_4$, $(HIO_3)_4(HIO_2)_3$, $(HIO_3)_3(HIO_2)_4$, $(H_2SO_4)_x(HIO_3)_y(HIO_2)_3$ ($x + y = 4$) and $(H_2SO_4)_x(HIO_3)_y(HIO_2)_4$ ($x + y = 3$) clusters were selected as boundary clusters that are allowed to leave the H_2SO_4-HIO_3-HIO_2 simulation system and contribute to cluster formation rates, and their physical diameters were estimated to be ~ 1.2 nm, which is comparable to the mass diameter of 1.4 nm for the reported nucleation rates of cloud experiments. The selection of $(H_2SO_4)_4(HIO_2)_4$ instead of $(H_2SO_4)_4(HIO_2)_3$ is due to the higher evaporation rate (7×10^{-2} s^{-1}) of the latter. As $(H_2SO_4)_4(HIO_2)_4$ has an evaporation rate of 3×10^{-5} s^{-1}, it is stable enough to be considered as the boundary cluster. Since the enhancement factor for collision rate coefficients of H_2SO_4 molecules from hard sphere kinetic gas theory is around 2.3 due to attractive van der Waals forces(*33*, *73*) and we approximately estimated the enhancement factor to be 2.4 for HIO_3-HIO_2 collision in our recent study(*28*), the enhancement factor is approximated to be 2.3 for H_2SO_4-HIO_3-HIO_2 system here. To compare directly with CLOUD experiments, the simulations were run under the same precursor concentrations (concentrations of HIO_3, H_2SO_4 and HIO_2) and wall loss rates as the CLOUD experiments for each cluster at −10 ℃ (Fig. 2C). In addition, we also ran ACDC simulations for the binary HIO_3-HIO_2 system and H_2SO_4-HIO_2 system using a "3 × 3" box as a comparison with the ternary H_2SO_4-HIO_3-HIO_2 system. $(HIO_3)_4(HIO_2)_3$ and $(HIO_3)_3(HIO_2)_4$, $(H_2SO_4)_3(HIO_2)_4$ and $(H_2SO_4)_4(HIO_2)_4$ clusters were set as the boundary clusters for HIO_3-HIO_2 system and H_2SO_4-HIO_2 system respectively, and other settings were similar to those of the H_2SO_4-HIO_3-HIO_2 system.

The formation mechanisms of HIO_2

Quantum chemical calculations were employed in order to investigate the formation mechanisms of iodous acid, HIO_2. The reactants, intermediates, transition states and products for reactions $I_2O_2 + H_2O \rightarrow HIO_2 + HOI$ (R1) and $OIO + HO_2 \rightarrow HIO_2 + O_2$ (R2) have multiple possible conformers. A systematic conformer sampling was carried out using the MMFF method in the Spartan '18 program. The conformer sampling algorithm with Spartan allows for pre-optimization and the elimination of duplicate structures, which is computationally more efficient than other conformer sampling approaches like MS-TOR. Geometry optimization and frequencies were calculated with M06-2X/aug-cc-pVTZ(-PP) method with the ultrafine grid using the Gaussian 16 program(*71*). This was followed by coupled-cluster single-point energy corrections at the CCSD(T)/aug-cc-pVTZ(-PP) level of theory using the ORCA 4.2.1 program(*74*). Iodine pseudopotentials were taken from the Environmental Molecular Sciences Laboratory (EMSL) basis set library(*75*, *76*). The stability of the wavefunction was checked at the CCSD(T) stage to ensure that the lowest lying wavefunction was found for the intermediates and transition states along R1 and R2. This was carried out by running Hartree-Fock calculations with 15 HOMOs ad 15 LUMOs switched randomly and generating 100 input files with the orbital rotations applied. These calculations were carried out with the def2-TZVPP basis set and using the ORCA program. This is a much more robust approach for checking wavefunction stability than e.g., the standard Stable=Opt check in Gaussian.

The formation of HIO_2 via R2 along the triplet surface was also checked and found to have a low barrier of ca. 2.5 kcal mol^{-1} above the intermediate (and –9.4 kcal mol^{-1} below the reactants OIO + HO_2). Additionally, this leads to the formation of a triplet O_2 (+singlet HIO_2), which is a significantly exothermic process (ca. –36 kcal mol^{-1} below the reactants). The triplet transition state also has a very low imaginary frequency of –45 cm^{-1}, which likely indicates that the reaction is close to barrierless.

Supplementary references

44. A. Dias, S. Ehrhart, A. Vogel, C. Williamson, J. Almeida, J. Kirkby, S. Mathot, S. Mumford, A. Onnela, Temperature uniformity in the CERN CLOUD chamber. *Atmospheric Measurement Techniques.* **10**, 5075–5088 (2017). doi:10.5194/amt-10-5075-2017

45. J. Duplissy, J. Merikanto, A. Franchin, G. Tsagkogeorgas, J. Kangasluoma, D. Wimmer, H. Vuollekoski, S. Schobesberger, K. Lehtipalo, R. C. Flagan, D. Brus, N. M. Donahue, H. Vehkamäki, J. Almeida, A. Amorim, P. Barmet, F. Bianchi, M. Breitenlechner, E. M. Dunne, R. Guida, H. Henschel, H. Junninen, J. Kirkby, A. Kürten, A. Kupc, A. Määttänen, V. Makhmutov, S. Mathot, T. Nieminen, A. Onnela, A. P. Praplan, F. Riccobono, L. Rondo, G. Steiner, A. Tome, H. Walther, U. Baltensperger, K. S. Carslaw, J. Dommen, A. Hansel, T. Petäjä, M. Sipilä, F. Stratmann, A. Vrtala, P. E. Wagner, D. R. Worsnop, J. Curtius, M. Kulmala, Effect of ions on sulfuric acid-water binary particle formation: 2. Experimental data and comparison with QC-normalized classical nucleation theory. *Journal of Geophysical Research: Atmospheres*. **121**, 1752–1775 (2016). doi:10.1002/2015JD023539

46. H. Junninen, M. Ehn, T. Petäjä, L. Luosujärvi, T. Kotiaho, R. Kostiainen, U. Rohner, M. Gonin, K. Fuhrer, M. Kulmala, D. R. Worsnop, A high-resolution mass spectrometer to measure atmospheric ion composition. *Atmospheric Measurement Techniques*. **3**, 1039–1053 (2010). doi:10.5194/amt-3-1039-2010

47. M. P. Rissanen, J. Mikkilä, S. Iyer, J. Hakala, Multi-scheme chemical ionization inlet (MION) for fast switching of reagent ion chemistry in atmospheric pressure chemical ionization mass spectrometry (CIMS) applications. *Atmospheric Meassurement Techniques.* **12**, 6635–6646 (2019). doi:10.5194/amt-12-6635-2019

48. H. E. Manninen, S. Mirme, A. Mirme, T. Petäjä, M. Kulmala, How to reliably detect molecular clusters and nucleation mode particles with Neutral cluster and Air Ion Spectrometer (NAIS). *Atmospheric Meassurement Techniques.* **9**, 3577–3605 (2016). doi:10.5194/amt-93577-2016

49. S. Mirme, A. Mirme, The mathematical principles and design of the NAIS – a spectrometer for the measurement of cluster ion and nanometer aerosol size distributions. *Atmospheric Meassurement Techniques.* **6**, 1061–1071 (2013). doi:10.5194/amt-6-1061-2013

50. J. Vanhanen, J. Mikkilä, K. Lehtipalo, M. Sipilä, H. E. Manninen, E. Siivola, T. Petäjä, M. Kulmala, Particle Size Magnifier for Nano-CN Detection. *Aerosol Science and Technology*. **45**, 533–542 (2011). doi:10.1080/02786826.2010.547889

51. J. Tröstl, T. Tritscher, O. F. Bischof, H.-G. Horn, T. Krinke, U. Baltensperger, M. Gysel, Fast and precise measurement in the sub-20nm size range using a Scanning Mobility Particle Sizer. *Journal of Aerosol Science*. **87**, 75–87 (2015). doi:10.1016/j.jaerosci.2015.04.001

52. D. Stolzenburg, G. Steiner, P. M. Winkler, A DMA-train for precision measurement of sub-10 nm aerosol dynamics. *Atmospheric Meassurement Techniques.* **10**, 1639–1651 (2017). doi:10.5194/amt10-1639-2017

53. M. Wang, X.-C. He, H. Finkenzeller, S. Iyer, D. Chen, J. Shen, M. Simon, V. Hofbauer, J. Kirkby, J. Curtius, N. Maier, T. Kurtén, D. R. Worsnop, M. Kulmala, M. Rissanen, R. Volkamer, Y. J. Tham, N. M. Donahue, M. Sipilä, Measurement of iodine species and sulfuric acid using bromide chemical ionization mass spectrometers. *Atmospheric Meassurement Techniques.* **14**, 4187–4202 (2021). doi:10.5194/amt-14-4187-2021

54. J. Pfeifer, M. Simon, M. Heinritzi, F. Piel, L. Weitz, D. Wang, M. Granzin, T. Müller, S. Bräkling, J. Kirkby, J. Curtius, A. Kürten, Measurement of ammonia, amines and iodine compounds using protonated water cluster chemical ionization mass spectrometry. *Atmospheric Measurement Techniques*. **13**, 2501–2522 (2020). doi:10.5194/amt-13-2501-2020

55. M. Breitenlechner, L. Fischer, M. Hainer, M. Heinritzi, J. Curtius, A. Hansel, PTR3: An Instrument for Studying the Lifecycle of Reactive Organic Carbon in the Atmosphere. *Analytical Chemistry.* **89**, 5824–5831 (2017). doi:10.1021/acs.analchem.6b05110

56. M. Wang, M. Xiao, B. Bertozzi, G. Marie, B. Rörup, B. Schulze, R. Bardakov, X.-C. He, J. Shen, W. Scholz, R. Marten, L. Dada, R. Baalbaki, B. Lopez, H. Lamkaddam, H. E. Manninen, A. Amorim, F. Ataei, P. Bogert, Z. Brasseur, L. Caudillo, L.-P. De Menezes, J. Duplissy, A. M. L. Ekman, H. Finkenzeller, L. G. Carracedo, M. Granzin, R. Guida, M. Heinritzi, V. Hofbauer, K. Höhler, K. Korhonen, J. E. Krechmer, A. Kürten, K. Lehtipalo, N. G. A. Mahfouz, V. Makhmutov, D. Massabò, S. Mathot, R. L. Mauldin, B. Mentler, T. Müller, A. Onnela, T. Petäjä, M. Philippov, A. A. Piedehierro, A. Pozzer, A. Ranjithkumar, M. Schervish, S. Schobesberger, M. Simon, Y. Stozhkov, A. Tomé, N. S. Umo, F. Vogel, R. Wagner, D. S. Wang, S. K. Weber, A. Welti, Y. Wu, M. Zauner-Wieczorek, M. Sipilä, P. M. Winkler, A. Hansel, U. Baltensperger, M. Kulmala, R. C. Flagan, J. Curtius, I. Riipinen, H. Gordon, J. Lelieveld, I. El-Haddad, R. Volkamer, D. R. Worsnop, T. Christoudias, J. Kirkby, O. Möhler, N. M. Donahue, Synergistic HNO_3–H_2SO_4–NH_3 upper tropospheric particle formation. *Nature*. **605**, 483–489 (2022). doi:10.1038/s41586-022-04605-4

57. T. Jokinen, M. Sipilä, H. Junninen, M. Ehn, G. Lönn, J. Hakala, T. Petäjä, R. L. Mauldin, M. Kulmala, D. R. Worsnop, Atmospheric sulphuric acid and neutral cluster measurements using CI-APi-TOF. *Atmospheric Chemistry and Physics*. **12**, 4117–4125 (2012). doi:10.5194/acp-12-4117-2012

58. A. Kürten, T. Jokinen, M. Simon, M. Sipilä, N. Sarnela, H. Junninen, A. Adamov, J. Almeida, A. Amorim, F. Bianchi, M. Breitenlechner, J. Dommen, N. M. Donahue, J. Duplissy, S. Ehrhart, R. C. Flagan, A. Franchin, J. Hakala, A. Hansel, M. Heinritzi, M. Hutterli, J. Kangasluoma, J. Kirkby, A. Laaksonen, K. Lehtipalo, M. Leiminger, V. Makhmutov, S. Mathot, A. Onnela, T. Petäjä, A. P. Praplan, F. Riccobono, M. P. Rissanen, L. Rondo, S. Schobesberger, J. H. Seinfeld, G. Steiner, A. Tomé, J. Tröstl, P. M. Winkler, C. Williamson, D. Wimmer, P. Ye, U. Baltensperger, K. S. Carslaw, M. Kulmala, D. R. Worsnop, J. Curtius, Neutral molecular cluster formation of sulfuric acid–dimethylamine observed in real time under atmospheric conditions. *Proceedings of the National Academy of Sciences*. **111**, 15019–15024 (2014). doi:10.1073/pnas.1404853111

59. A. Kürten, L. Rondo, S. Ehrhart, J. Curtius, Calibration of a Chemical Ionization Mass Spectrometer for the Measurement of Gaseous Sulfuric Acid. *Journal of Physical Chemistry A*. **116**, 6375–6386 (2012). doi:10.1021/jp212123n

60. B. K. Ku, J. F. de la Mora, Relation between Electrical Mobility, Mass, and Size for Nanodrops 1–6.5 nm in Diameter in Air. *Aerosol Science and Technology*. **43**, 241–249 (2009). doi:10.1080/02786820802590510

61. L. Dada, K. Lehtipalo, J. Kontkanen, T. Nieminen, R. Baalbaki, L. Ahonen, J. Duplissy, C. Yan, B. Chu, T. Petäjä, K. Lehtinen, V.-M. Kerminen, M. Kulmala, J. Kangasluoma, Formation and growth of sub-3-nm aerosol particles in experimental chambers. *Nature Protocols*. **15**, 1013–1040 (2020). doi:10.1038/s41596-019-0274-z

62. K. Lehtipalo, J. Leppa, J. Kontkanen, J. Kangasluoma, A. Franchin, D. Wimnner, S. Schobesberger, H. Junninen, T. Petaja, M. Sipila, others, Methods for determining particle size distribution and growth rates between 1 and 3 nm using the Particle Size Magnifier. *Boreal Environment Research*. **19**, 215–236 (2014).

63. V.-M. Kerminen, M. Kulmala, Analytical formulae connecting the "real" and the "apparent" nucleation rate and the nuclei number concentration for atmospheric nucleation events. *Journal of Aerosol Science*. **33**, 609–622 (2002). doi:10.1016/S0021-8502(01)00194-X

64. K. E. J. Lehtinen, M. Dal Maso, M. Kulmala, V.-M. Kerminen, Estimating nucleation rates from apparent particle formation rates and vice versa: Revised formulation of the Kerminen–Kulmala equation. *Journal of Aerosol Science*. **38**, 988–994 (2007). doi:10.1016/j.jaerosci.2007.06.009

65. R. C. Thakur, L. Dada, L. J. Beck, L. L. J. Quéléver, T. Chan, M. Marbouti, X.-C. He, C. Xavier, J. Sulo, J. Lampilahti, M. Lampimäki, Y. J. Tham, N. Sarnela, K. Lehtipalo, A. Norkko, M. Kulmala, M. Sipilä, T. Jokinen, An evaluation of new particle formation events in Helsinki during a Baltic Sea cyanobacterial summer bloom. *Atmospheric Chemistry and Physics.* **22**, 6365–6391 (2022). doi:10.5194/acp-22-6365-2022

66. T. Jokinen, K. Lehtipalo, R. C. Thakur, I. Ylivinkka, K. Neitola, N. Sarnela, T. Laitinen, M. Kulmala, T. Petäjä, M. Sipilä, Measurement report: Long-term measurements of aerosol precursor concentrations in the Finnish subarctic boreal forest. *Atmospheric Chemistry and Physics.* **22**, 2237–2254 (2022). doi:10.5194/acp-22-2237-2022

67. H.-B. Xie, J. Elm, R. Halonen, N. Myllys, T. Kurtén, M. Kulmala, H. Vehkamäki, Atmospheric Fate of Monoethanolamine: Enhancing New Particle Formation of Sulfuric Acid as an Important Removal Process. *Environmental Science Technology.* **51**, 8422–8431 (2017). doi:10.1021/acs.est.7b02294

68. J. Shen, H.-B. Xie, J. Elm, F. Ma, J. Chen, H. Vehkamäki, Methanesulfonic Acid-driven New Particle Formation Enhanced by Monoethanolamine: A Computational Study. *Environmental Science Technology.* **53**, 14387–14397 (2019). doi:10.1021/acs.est.9b05306

69. R. Zhang, J. Shen, H.-B. Xie, J. Chen, J. Elm, The role of organic acids in new particle formation from methanesulfonic acid and methylamine. *Atmospheric Chemistry and Physics.* **22**, 2639–2650 (2022). doi:10.5194/acp-22-2639-2022

70. I. Funes-Ardoiz, R. S. Paton, Goodvibes: Goodvibes V1.0.1, Zenodo (2016); https://doi.org/10.5281/zenodo.60811.

71. M. J. Frisch, G. W. Trucks, H. B. Schlegel, G. E. Scuseria, M. A. Robb, J. R. Cheeseman, G. Scalmani, V. Barone, G. A. Petersson, H. Nakatsuji, X. Li, M. Caricato, A. V. Marenich, J. Bloino, B. G. Janesko, R. Gomperts, B. Mennucci, H. P. Hratchian, J. V. Ortiz, A. F. Izmaylov, J. L. Sonnenberg, Williams, F. Ding, F. Lipparini, F. Egidi, J. Goings, B. Peng, A. Petrone, T. Henderson, D. Ranasinghe, V. G. Zakrzewski, J. Gao, N. Rega, G. Zheng, W. Liang, M. Hada, M. Ehara, K. Toyota, R. Fukuda, J. Hasegawa, M. Ishida, T. Nakajima, Y. Honda, O. Kitao, H. Nakai, T. Vreven, K. Throssell, J. A. Montgomery Jr., J. E. Peralta, F. Ogliaro, M. J. Bearpark, J. J. Heyd, E. N. Brothers, K. N. Kudin, V. N. Staroverov, T. A. Keith, R. Kobayashi, J. Normand, K. Raghavachari, A. P. Rendell, J. C. Burant, S. S. Iyengar, J. Tomasi, M. Cossi, J. M. Millam, M. Klene, C. Adamo, R. Cammi, J. W. Ochterski, R. L. Martin, K. Morokuma, O. Farkas, J. B. Foresman, D. J. Fox, Gaussian 16, Revision C.01 (Gaussian, Inc., 2016).

72. F. Neese, The ORCA program system: The ORCA program system. *Wiley Interdisciplinary Reviews: Computational Molecular Science*. **2**, 73–78 (2012). doi:10.1002/wcms.81

73. R. Halonen, E. Zapadinsky, T. Kurtén, H. Vehkamäki, B. Reischl, Rate enhancement in collisions of sulfuric acid molecules due to long-range intermolecular forces. *Atmospheric Chemistry and Physics.* **19**, 13355–13366 (2019). doi:10.5194/acp-19-13355-2019

74. F. Neese, F. Wennmohs, U. Becker, C. Riplinger, The ORCA quantum chemistry program package. *Journal of Chemical Physics.* **152**, 224108 (2020). doi:10.1063/5.0004608

75. D. Feller, The role of databases in support of computational chemistry calculations. *Journal of Computational Chemistry*. **17**, 1571–1586 (1996). doi:10.1002/(SICI)1096-987X(199610)17:13<1571:AID-JCC9>3.0.CO;2-P

76. K. A. Peterson, D. Figgen, E. Goll, H. Stoll, M. Dolg, Systematically convergent basis sets with relativistic pseudopotentials. II. Small-core pseudopotentials and correlation consistent basis sets for the post- *d* group 16–18 elements. *Journal of Chemical Physics*. **119**, 11113–11123 (2003). doi:10.1063/1.1622924

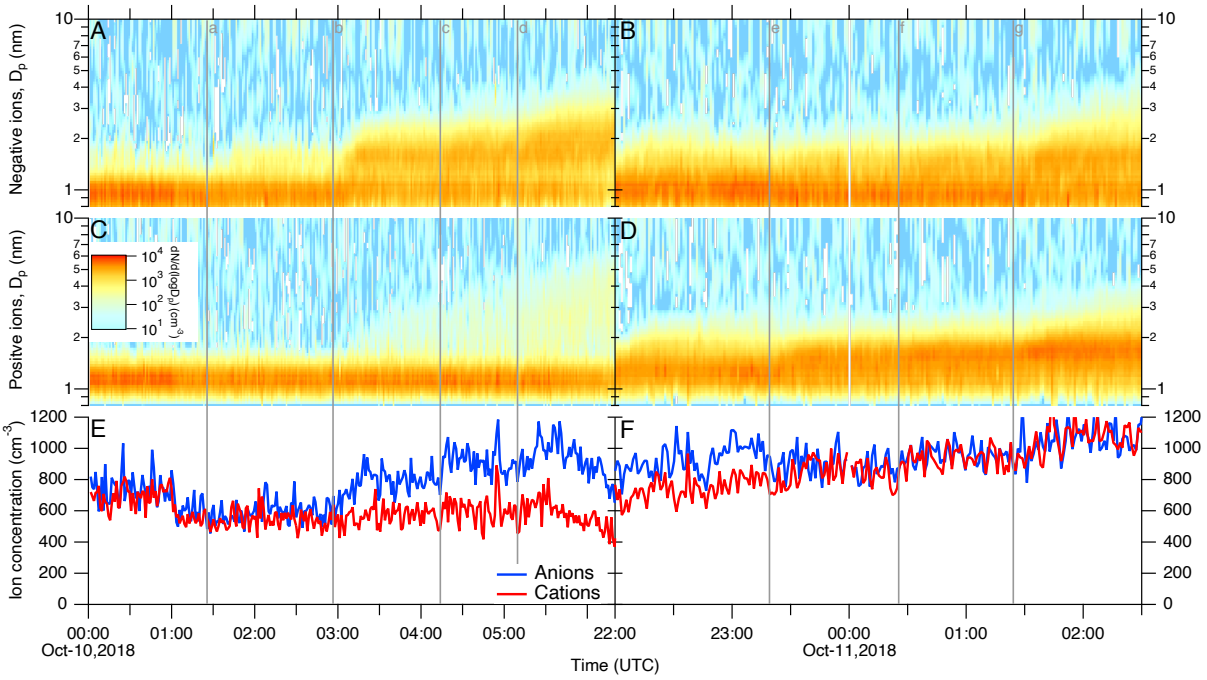

Fig. S1. Ion number size distribution from HIO_x-H_2SO_4 (A, C, E) and HIO_x-H_2SO_4-NH_3 (B, D, F) at -10 °C. (A, B) Negative ion number size distribution, (C, D) positive ion number size distribution and (E, F) ion concentrations. Ion-induced nucleation at background level of NH_3 levels only occurs at the negative channel (A) and the negative ion concentration is significantly higher than positive ions (E). However, ion-induced nucleation turns to bipolar (B, D) at ca. 40 pptv of NH_3 and the ion concentrations at both polarities are similar. The experimental conditions are the same as in Fig. 1: 41.1 ppbv O_3, 63.5% RH, 2.3 ppbv SO_2 and 17.4 pptv I_2 (A, C, E), and 40.8 ppbv O_3, 62.3% RH, 1.6 ppbv SO_2 and 67.2 pptv I_2 (B, D, F) with varying light intensities. Stages (a, c, d, e, f, g) enhanced the UVH light intensity (higher OH production rates) and stage (b) increased the green light intensity (higher I_2 photolysis rate). The results suggest that ion-induced HIO_x-H_2SO_4 nucleation proceeds in the negative channel, while ion-induced HIO_x-H_2SO_4-NH_3 nucleation proceeds in both the negative and positive channels.

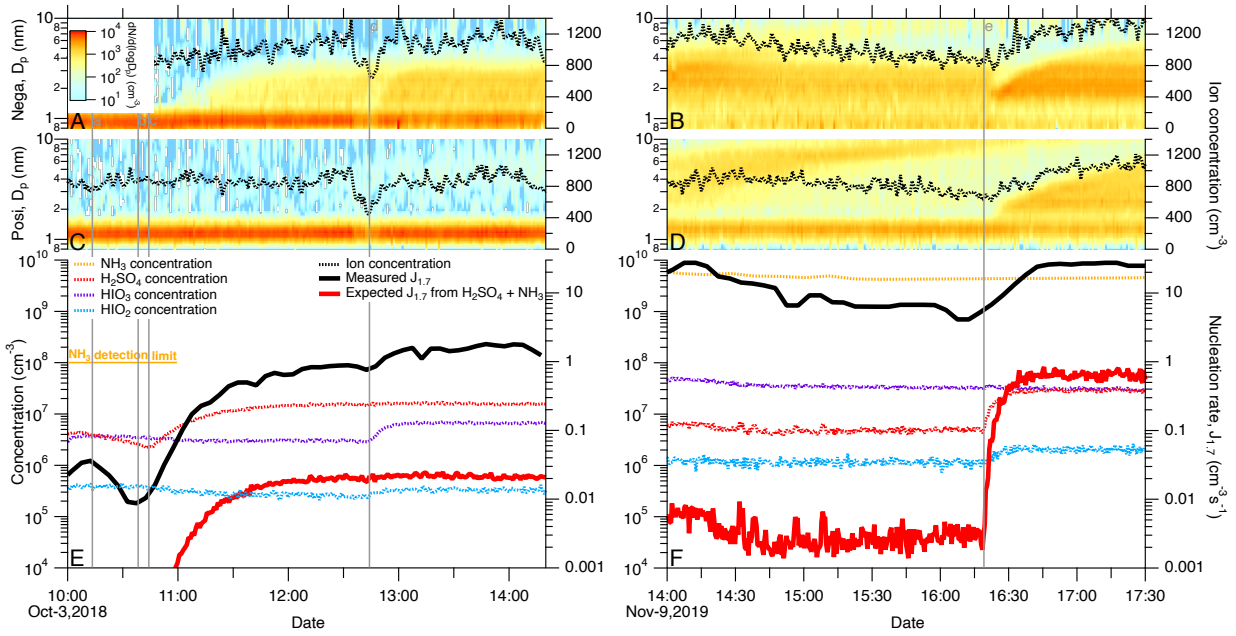

Fig. S2. New particle formation from HIO_x-H_2SO_4 (A, C, E) and HIO_x-H_2SO_4-NH_3 (B, D, F) at 10 °C. (A, B) Negative ion number size distribution, (C, D) positive ion number size distribution and (E, F) vapor concentrations and nucleation rates. Solid lines show measured nucleation rates at 1.7 nm, $J_{1.7}$ (solid black) and predicted $J_{1.7}$ from H_2SO_4-NH_3 nucleation alone (solid red)(*14*). Dashed lines represent ion and vapor concentrations. The NH_3 concentration in panel E is the detection limit of H_3O^+-CIMS instrument(*54*) and the actual NH_3 concentration is expected to be below 1 pptv as all charged clusters are essentially NH_3 free (Fig. 3).The experimental conditions are 42.7 ppbv O_3, 75.3 % RH, 1.8 ppbv SO_2 and 27.4 pptv I_2 (A, C, E), and 43.3 ppbv O_3, 42.4 % RH and 0.6 ppbv SO_2 (B, D, F). I_2 concentration was not measured at 10 ºC. Vertical grey bars (a-c) show the experimental stages of increasing SO_2 concentrations, (d) represents elevating the green light intensity, (e) indicates elevating both the green light and UVH intensities. The experiments clearly show that HIO_x significantly enhances H_2SO_4-NH_3 nucleation at comparable HIO_3 and H_2SO_4 concentrations at 10 °C. Additionally, ion-induced nucleation at background NH_3 levels only occurs at the negative channel (A) but it turns to bipolar (B, D) at ca. 200 pptv of NH_3.

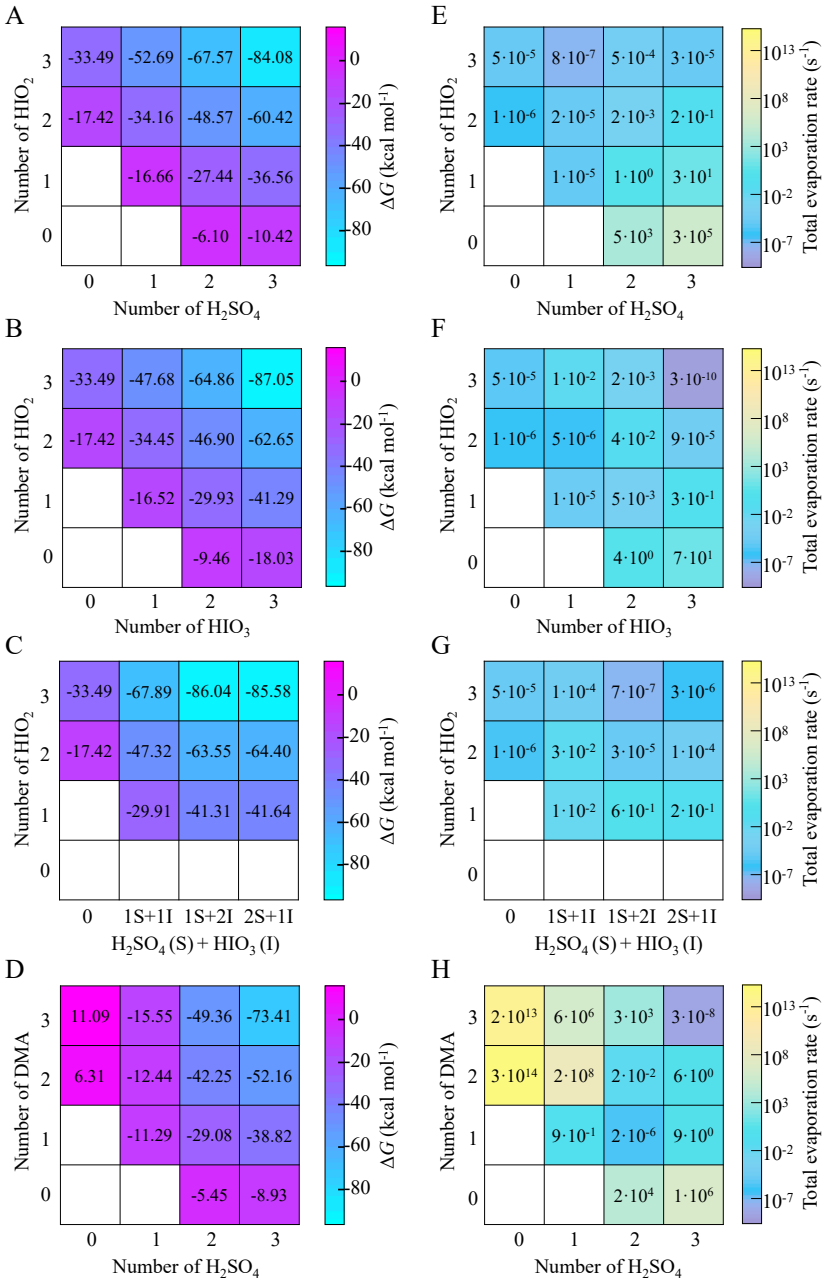

Fig. S3. Formation free energy and evaporation rate. Formation free energy (ΔG) of A) $(H_2SO_4)_m(HIO_2)_n$, B) $(HIO_3)_m(HIO_2)_n$, C) $(HIO_3{+}H_2SO_4)_m(HIO_2)_n$ and D) $(SA)_m(DMA)_n$ (data adopted from Xie et al. 2017(*67*)) clusters (m = 0-3, n = 0-3) calculated at the DLPNO-CCSD(T)/aug-cc-pVTZ(-PP)//M06-2X/aug-cc-pVTZ(-PP) (A, B, C) and DLPNO-CCSD(T)/aug-cc-pVTZ//ωB97X-D/6-31++G(d,p) (D) levels, respectively. The calculations are performed at 25 °C and 1 atm. Evaporation rates of the E) $(HIO_3)_m(HIO_2)_n$, F) $(H_2SO_4)_m(HIO_2)_n$, G) $(HIO_3{+}H_2SO_4)_m(HIO_2)_n$ and H) $(H_2SO_4)_m(DMA)_n$ clusters at −10 °C and 1 atm. The results show that the HIO_3-HIO_2, H_2SO_4-HIO_2 and H_2SO_4-HIO_3-HIO_2 clusters are extremely stable.

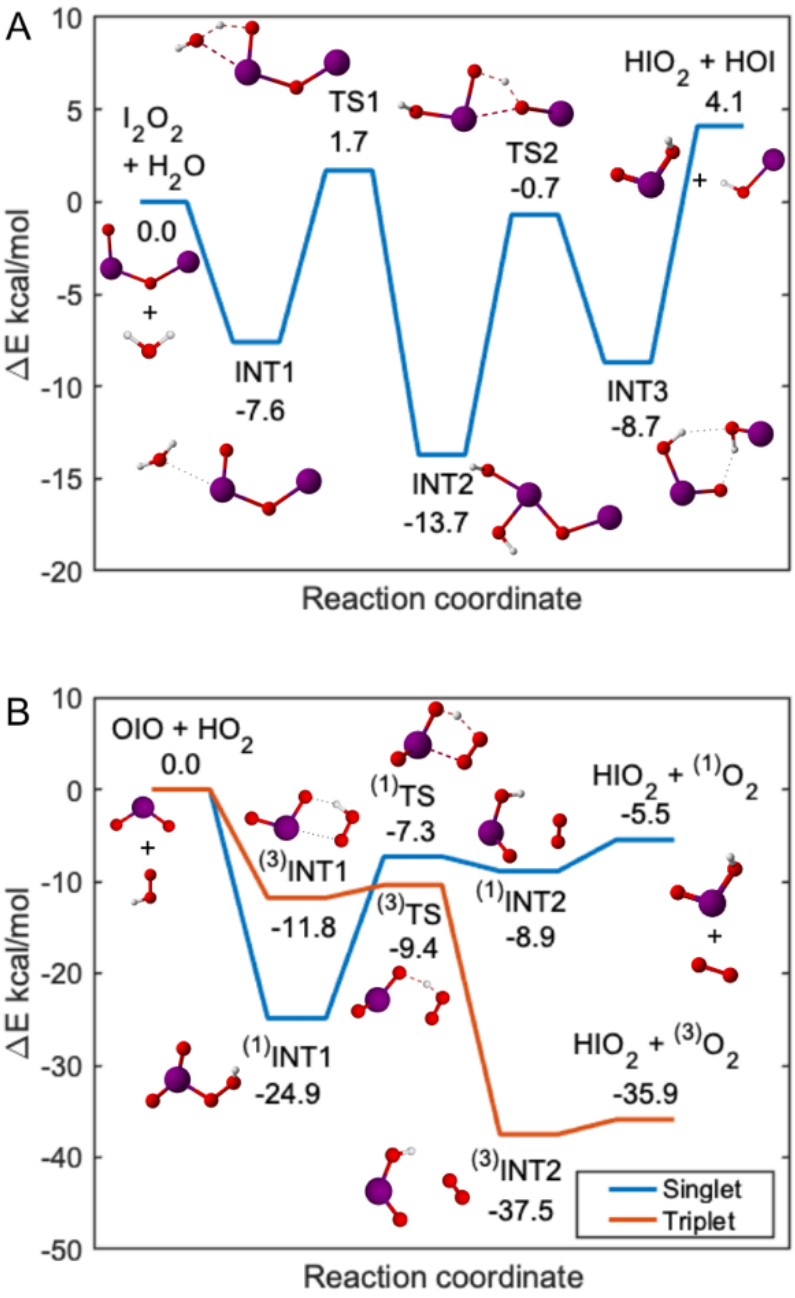

Fig. S4. Gas-phase formation mechanisms of HIO_2. A) Stationary points along the potential energy surface of reaction $I_2O_2 + H_2O \rightarrow HIO_2 + HOI$ and B) Stationary points along the potential energy surface of reaction $OIO + HO_2 \rightarrow HIO_2 + {}^{(1,3)}O_2$. Zero-point corrected energies are shown on the y-axis and the reaction coordinate on the x-axis. Color coding: Purple – iodine, red – oxygen, white – hydrogen. Our results indicate that $I_2O_2 + H_2O$ and $OIO + HO_2$ are potential reactions forming HIO_2 in the gas phase.

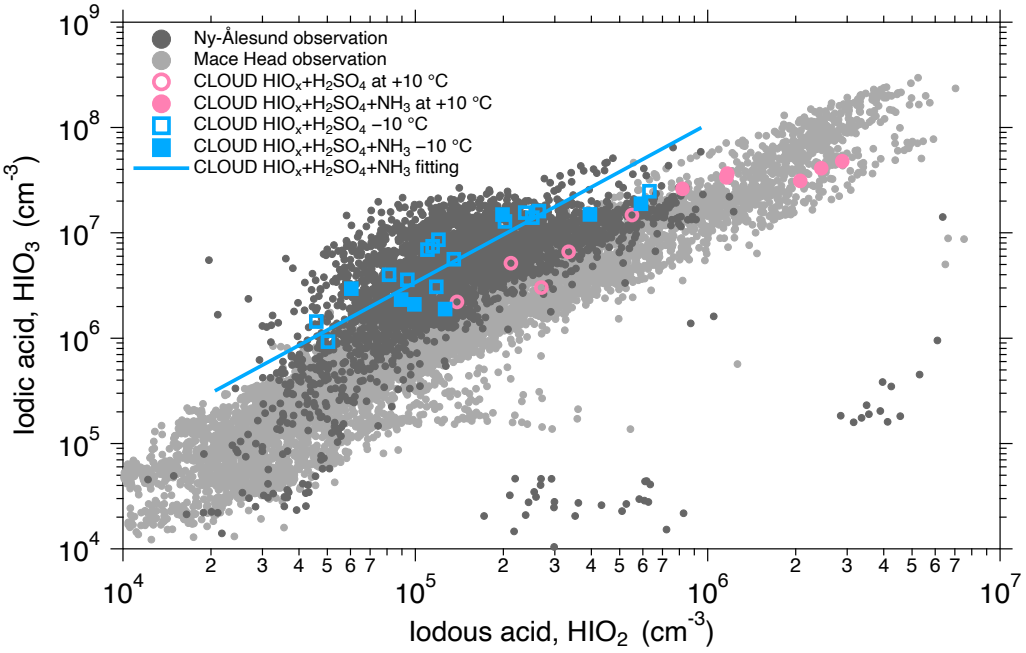

Fig. S5. HIO_3 vs HIO_2 in CLOUD and field observations. The Ny-Ålesund and Mace Head data sets are adopted from our earlier studies(*17*, *21*). HIO_x-H_2SO_4(-NH_3) experiments are the same as the ones presented in Fig. 2. The solid blue line is a fitting to the CLOUD data at −10 °C with an expression of $\log_{10}(HIO_2) = 0.6656 \times \log_{10}(HIO_3) + 0.6533$. The average temperature at Mace Head during September 2013 was around 14 °C and the temperature at Ny-Ålesund in March – August 2017 was between −19 and 10 °C. Our results show that both the ratio and absolute concentrations of HIO_2 and HIO_3 fall within the range measured at Mace Head and Ny-Ålesund.

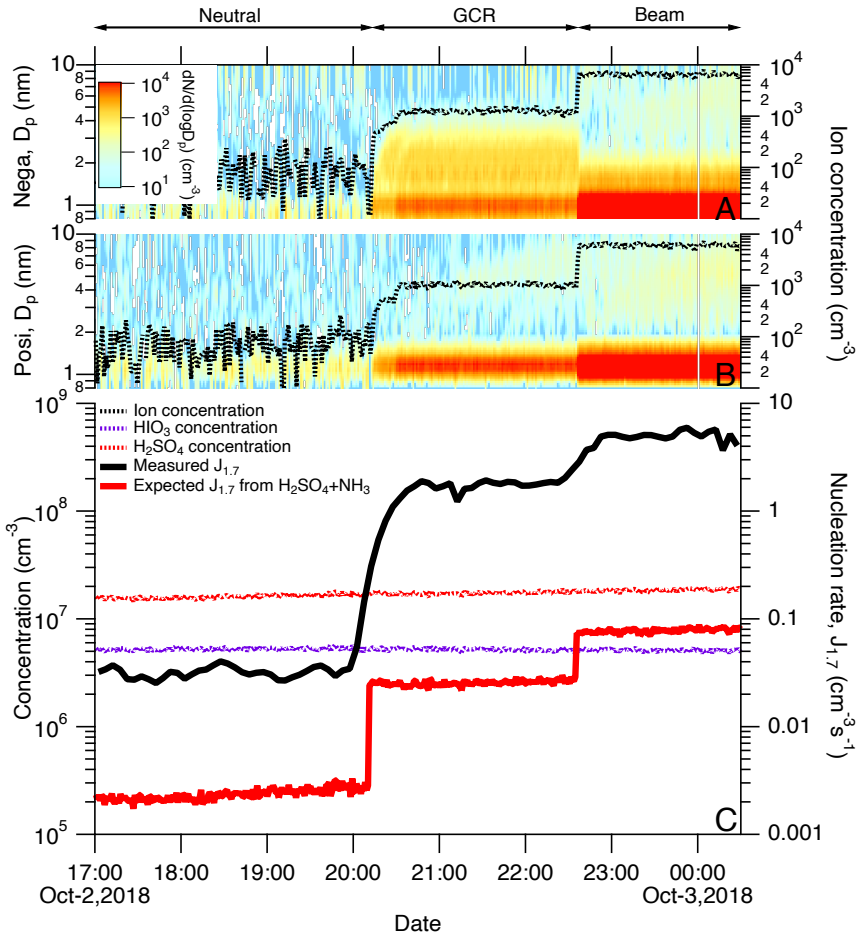

Fig. S6. Effect of ions on HIO_x-H_2SO_4 nucleation at 10 °C. (A) Negative ion size distribution, (B) positive ion size distribution and (C) vapor concentrations and nucleation rates. Solid lines show measured nucleation rates at 1.7 nm, $J_{1.7}$ (solid black) and predicted $J_{1.7}$ from H_2SO_4-NH_3 nucleation alone (solid red)(*14*). Dashed lines represent ion and vapor concentrations. The experiments were carried out at the beginning at ion-free conditions (neutral) and were continued at galactic cosmic ray conditions (GCR) and finally at beam enhancement conditions (Beam). The ion production rate enhancement at the beam condition is estimated by the ratio of ion concentrations from the beam condition to those from the GCR condition. A significant ion effect is observed in this set of experiments. The experimental conditions are 42.5 ppbv O_3, 75.2 % RH and 4.5 ppbv SO_2. Our results suggest that ground level of ionization rate significantly enhances HIO_x-H_2SO_4 nucleation while further enhanced ionization rate only moderately enhances the nucleation rate.

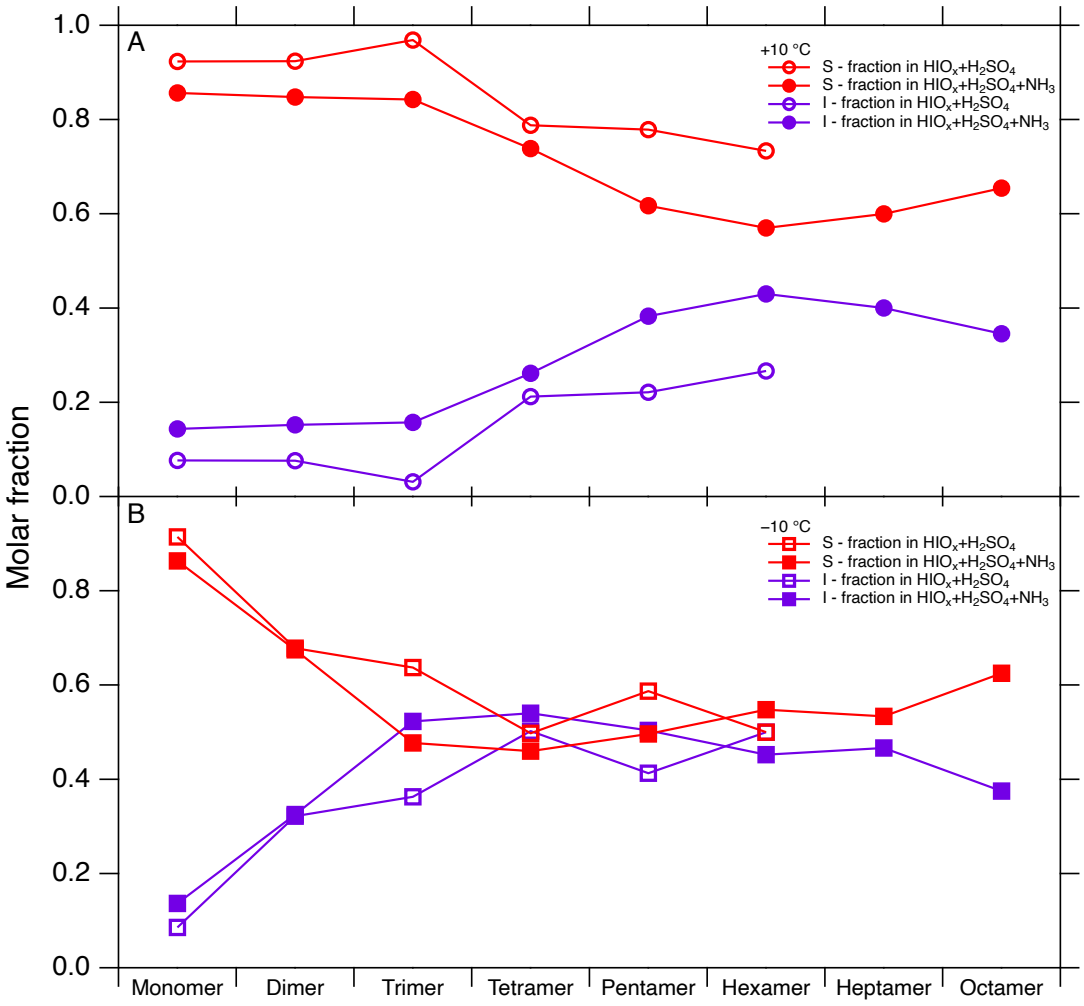

Fig. S7. Molar fraction of iodine and sulfur atoms. The oligomer number is defined as the sum of iodine and sulfur atoms (I + S) in a cluster and only these two atoms are used in the statistics. Red markers and lines represent sulfur atom molar fractions and purple markers and lines represent iodine atom molar fractions. (A) experiments done at 10 °C and (B) experiments carried out at −10 °C. The HIO_3:H_2SO_4 ratios are hollow circles ($5.0 \times 10^6 : 1.7 \times 10^7$), filled circles ($3.1 \times 10^7 : 2.8 \times 10^7$), hollow squares ($6.5 \times 10^6 : 6.9 \times 10^6$) and filled squares ($2.3 \times 10^6 : 1.6 \times 10^6$) (all numbers in unit of cm^{-3}). The data used for the statistics are the same as the ones presented in Fig. 3C, D, E and F. The results show that HIO_3 enhances H_2SO_4 stability in charged clusters under background NH_3 levels. At equal amounts of HIO_3 and H_2SO_4, NH_3 does not further enhance the H_2SO_4 molar ratio. Additionally, HIO_3 contributes to charged cluster formation starting at dimers at −10 °C and at tetramers at 10 °C.

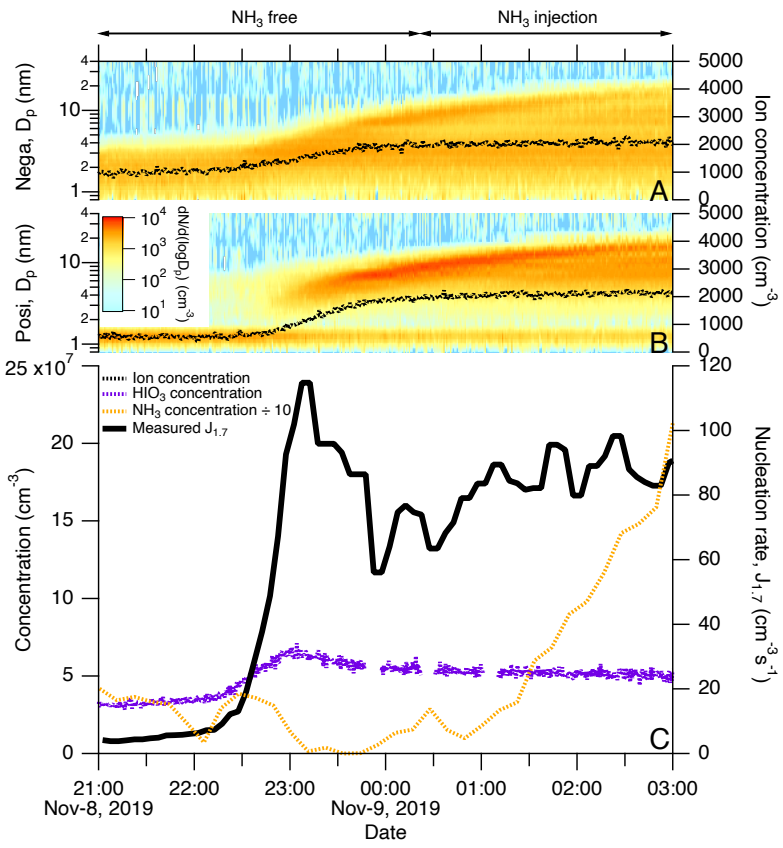

Fig. S8. Effect of NH_3 on HIO_x nucleation. (A) Negative ion size distribution, (B) positive ion size distribution and (C) vapor concentrations and nucleation rates. The results show that NH_3 has a negligible effect on HIO_x nucleation. Dashed lines represent total ion concentrations (dashed black), HIO_3 concentrations (dashed purple) and NH_3 concentrations (dashed yellow). The NH_3 concentrations are scaled down by a factor of 10 to optimize data presentation. The solid black line shows measured nucleation rates at 1.7 nm, $J_{1.7}$. The experimental conditions are 42.1 ppbv O_3 and 43.3 % RH. The results show that NH_3 up to 100 pptv does not significantly enhance iodine oxoacid nucleation.

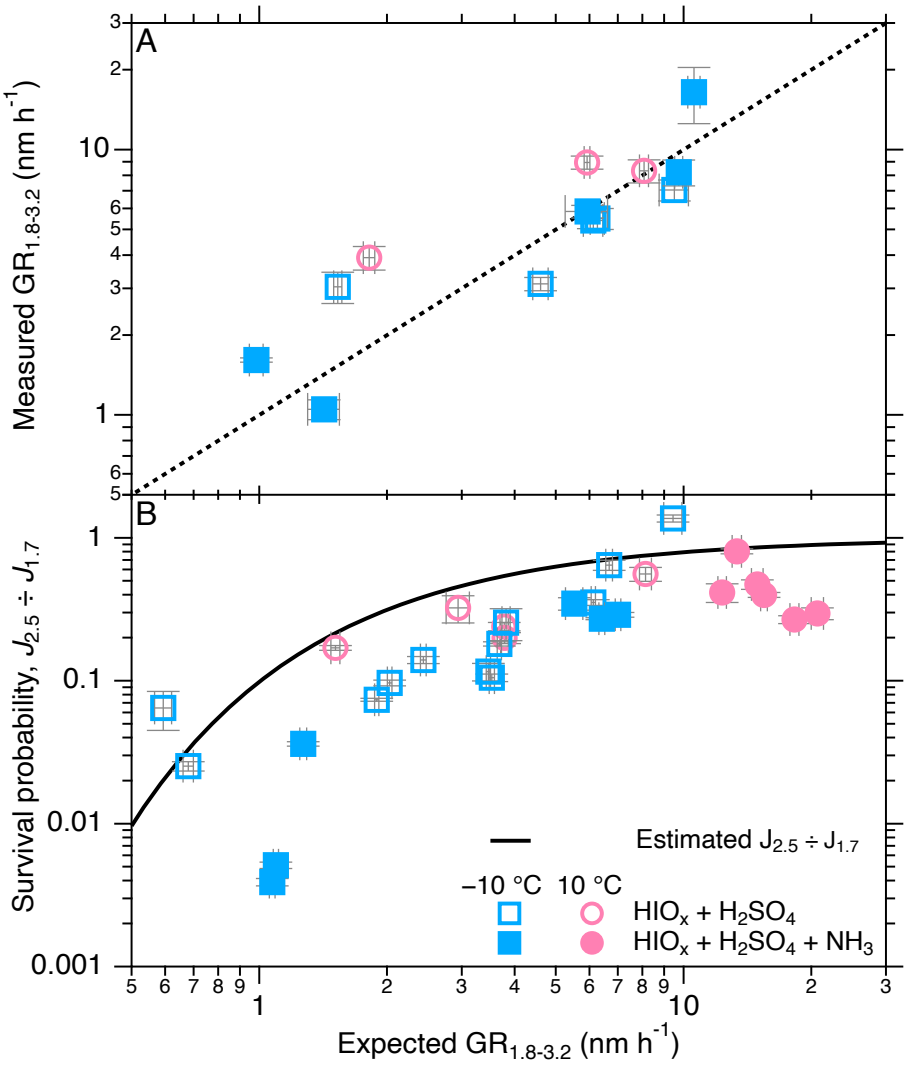

Fig. S9. Growth rate and survival probability. (A) measured growth rates between 1.8 to 3.2 nm by DMA-train versus the expected growth rates from kinetic H_2SO_4(*33*) and HIO_3(*18*) condensation at the concentrations corresponding to the measurement conditions. (B) survival probability of 1.7 nm particle growing to 2.5 nm, $J_{2.5}$ / $J_{1.7}$. The $J_{2.5}$ is measured with a condensation particle counter and the $J_{1.7}$ is measured with a particle size magnifier. The estimated survival probability is calculated based on Lehtinen et al.(*63*, *64*). Error bars show one standard deviation during the data selection period. Systematic errors resulting from uncertainties in the vapor concentrations (for estimating growth rates) and instrument cut-off sizes are not included in the plots. The results show that HIO_3 enhances H_2SO_4 stability in charged clusters under background NH_3 levels. At equal amounts of HIO_3 and H_2SO_4, NH_3 does not further enhance the H_2SO_4 molar ratio. Additionally, HIO_3 contributes to charged cluster formation starting at dimers at −10 °C and at tetramers at 10 °C.

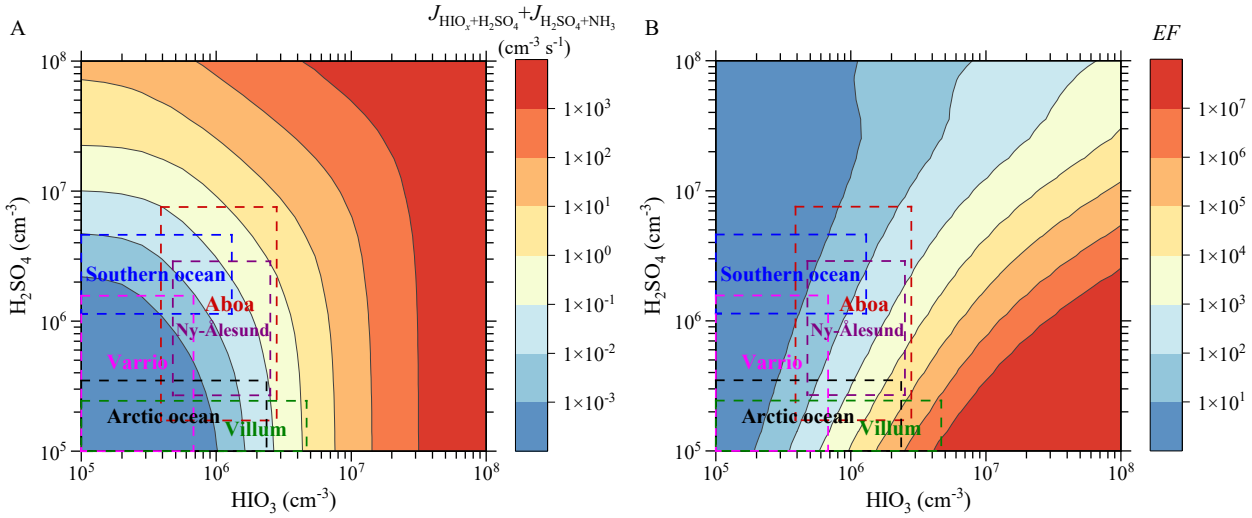

Fig. S10. Nucleation rate of HIO_x-H_2SO_4(-NH_3) and the enhancement by HIO_x at −10 °C. A) nucleation rate of HIO_x-H_2SO_4(+NH_3) estimated by summing up HIO_x-H_2SO_4 and H_2SO_4-NH_3 nucleation rates. The NH_3 concentration is assumed to be 10 pptv in pristine environments and the HIO_2 concentration is fitted from the experiments carried out at −10 °C (squares in Fig. S5). The condensation sink is assumed to be 0.0022 s^{-1} in the calculations. The nucleation rate of H_2SO_4-NH_3 is calculated from our earlier studies(*14*). The 10 % and 90 % ranges from polar observations are drawn on top of the nucleation rates by dashed lines. B) Nucleation rate enhancement factor (*EF*), is calculated by dividing the nucleation rate from the sum of HIO_x-H_2SO_4 and H_2SO_4-NH_3 (10 pptv) nucleation rates to the H_2SO_4-NH_3 nucleation rate alone. The 10 and 90 percentiles from polar observations are drawn on top of the EF indicating that the nucleation rates might be significantly underestimated if not considering HIO_x. The results show H_2SO_4-NH_3 nucleation might be significantly enhanced by HIO_x under ambient conditions.